

1 **Time-Of-Flight monitoring reveals higher sediment redistribution rates related to burrowing animals**
2 **than previously assumed**

3

4 *Paulina Grigusova*¹, *Annegret Larsen*², *Sebastian Achilles*¹, *Roland Brandl*³, *Camilo del Río*^{4,5}, *Nina Farwig*⁶,
5 *Diana Kraus*⁶, *Leandro Paulino*⁷, *Patricio Plissock*^{4,8,9}, *Kirstin Übernickel*¹⁰, *Jörg Bendix*¹

6

7

8 ¹ Laboratory for Climatology and Remote Sensing, Department of Geography, University of Marburg, 35037
9 Marburg, Germany; paulina.grigusova@staff.uni-marburg.de (P.G.); bendix@geo.uni-marburg.de (J.B.)

10 ² Soil Geography and Landscape, Department of Environmental Sciences,
11 Wageningen University & Research, 6700 AA Wageningen, The Netherlands; annegret.larsen@wur.nl

12 ³ Animal Ecology, Department of Biology, University of Marburg, 35032 Marburg, Germany;
13 brandlr@biologie.uni-marburg.de

14 ⁴ Facultad de Historia, Geografía y Ciencia Política, Instituto de Geografía, Pontificia Universidad Católica de
15 Chile, 782-0436 Santiago, Chile; plissock@uc.cl; cdelriol@uc.cl

16 ⁵ Centro UC Desierto de Atacama, Pontificia Universidad Católica de Chile, 782-0436 Santiago, Chile;
17 cdelriol@uc.cl

18 ⁶ Conservation Ecology, Department of Biology, University of Marburg, 35047 Marburg, Germany;
19 diana.kraus@biologie.uni-marburg.de (D.K.); nina.farwig@biologie.uni-marburg.de (N.F.)

20 ⁷ Facultad de Agronomía, Universidad de Concepción, 3780000 Chillán, Chile; lpaulino@udec.cl

21 ⁸ Facultad de Ciencias Biológicas, Departamento de Ecología, Pontificia Universidad Católica de Chile, 8331150
22 Santiago, Chile; plissock@uc.cl

23 ⁹ Center of Applied Ecology and Sustainability (CAPES), Pontificia Universidad Católica de Chile, 8331150
24 Santiago, Chile; plissock@uc.cl

25 ¹⁰ Earth System Dynamics, Department of Geosciences, University of Tübingen, 72076 Tübingen, Germany;
26 kirstin.uebernickel@uni-tuebingen.de

27

28 *Corresponding author:*

29 Paulina Grigusova

30 paulina.grigusova@staff.uni-marburg.de

31

32

33

34

35

36

37

38

39

40

41 **Abstract**

42 Burrowing animals influence surface microtopography and hillslope sediment redistribution, but changes often
43 remain undetected due to a lack of automated high resolution field monitoring techniques. In this study, we
44 present a new approach to quantify microtopographic variations and surface changes caused by burrowing
45 animals and rainfall-driven erosional processes applied to remote field plots in arid and mediterranean Chile.
46 We compared the mass balance of redistributed sediment within plot areas affected and not affected by
47 burrowing animals, quantified the cumulative sediment redistribution caused by animals and rainfall, and
48 upscaled the results to a hillslope scale. The newly developed instrument, a Time-of-Flight camera, showed a
49 very good detection accuracy. The animal-caused cumulative sediment redistribution was $14.62 \text{ cm}^3 \text{ cm}^{-2} \text{ year}^{-1}$
50 ¹ in the mediterranean and $9.57 \text{ } 16.41 \text{ cm}^3 \text{ cm}^{-2} \text{ year}^{-1}$ in the arid climate zone. The rainfall-caused cumulative
51 sediment redistribution within areas affected by burrowing animals was higher ($-10.44 \text{ cm}^3 \text{ cm}^{-2} \text{ year}^{-1}$) in the
52 mediterranean than the arid climate zone ($-1.41 \text{ cm}^3 \text{ cm}^{-2} \text{ year}^{-1}$). Daily sediment redistribution during rainfall
53 within areas affected by burrowing animals were up to 350% / 40% higher in the mediterranean / arid zone
54 compared to the unaffected areas, and much higher than previously reported in studies not based on continuous
55 microtopographic monitoring. Furthermore, 38% of the sediment eroding from the burrows accumulated within
56 the burrow entrance while 62% was incorporated into overall hillslope sediment flux. The animals burrowed
57 between on average 1.2 – 2.3 times a month and the burrowing intensity increased after rainfall. Our findings
58 can be implemented into long-term soil erosion models that rely on soil processes but do not yet include animal-
59 induced surface processes on microtopographical scales in their algorithms.

60

61 **Keywords:** Biogeomorphology, bioturbation, sediment transport, burrowing animals, rainfall, Time-of-Flight
62 camera, Chile

63

64

65

66

67

68

69

70

71

72

73

74

75

76

77

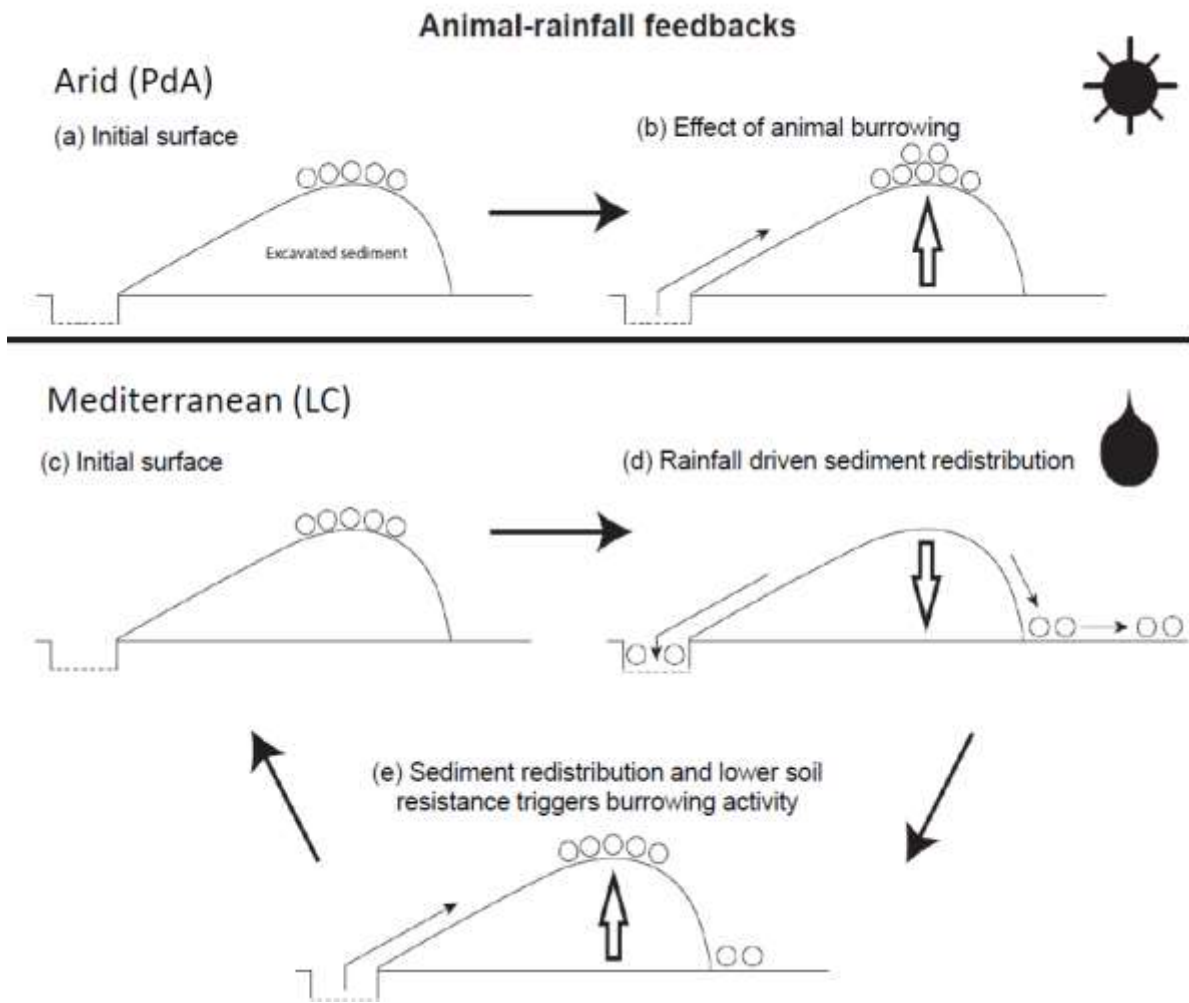
78

79

80

81

82 Graphical abstract



83

84

85 1. Introduction

86 Animal burrowing activity affects surface microtopography (Reichman and Seabloom, 2002; Kinlaw
87 and Grasmueck, 2012), surface roughness (Yair, 1995; Jones et al., 2010; Hancock and Lowry, 2021) and soil
88 physical properties (Ridd, 1996; Yair, 1995; Hall et al., 1999; Reichman and Seabloom, 2002; Hancock and
89 Lowry, 2021; Coombes, 2016; Larsen et al., 2021; Corenblit et al., 2021). Previous studies estimated both
90 positive as well as negative impacts of burrowing animals on sediment redistribution rates. The results were
91 obtained by applying tests under laboratory conditions using rainfall simulators, conducting several field
92 campaigns weeks to months apart, or by measuring the volume of excavated or eroded sediment in the field
93 using methods such as erosion pins, splash boards, or simple rulers (Imeson and Kwaad, 1976; Reichman
94 and Seabloom, 2002; Wei et al., 2007; Le Hir et al., 2007; Li et al., 2018; Li et al., 2019b; Li et al., 2019c;
95 Voiculescu et al., 2019; Chen et al., 2021; Übernickel et al., 2021a; Li et al., 2019a). Although burrowing
96 animals are generally seen as ecosystem engineers (Gabet et al., 2003; Wilkinson et al., 2009), their role in
97 soil erosion, in general, and for numerical soil erosion models, in particular, is, to date, limited to predictions of
98 the burrow locations and particle mixing at these locations (Black and Montgomery, 1991; Meysman et al.,
99 2003; Yoo et al., 2005; Schiffers et al., 2011). The complex interaction of sediment excavation and
100 accumulation, and erosion processes at the burrow and hillslope scales are not yet included in the modelling,
101 as for this, a suitable method capable of measuring all occurred redistribution processes is needed.

102 The reason for this knowledge gap is that previous studies have not provided data on low magnitude
103 but frequently occurring sediment redistribution due to the specific limitations of their approaches. Field
104 experiments with, for example, rainfall simulators can unveil processes but cannot cover the time-dependant
105 natural dynamics of sediment redistribution. For data samplings that used methods such as erosion pins or
106 splash boards, the sites had to be revisited each time and the data were thus obtained only sporadically
107 (Imeson and Kwaad, 1976; Hazelhoff et al., 1981; Richards and Humphreys, 2010). Similarly, estimations of
108 the excavated sediment volume are currently limited to one-time measurements or studies conducted several
109 months apart (Black and Montgomery, 1991; Hall et al., 1999; Yoo et al., 2005). We expect that non-
110 continuously conducted measurements do not include all frequently occurring excavation and erosion
111 processes. For this, a spatio-temporally high-resolution and continuous monitoring of sediment redistribution
112 is needed.

113 High-resolution, ground-based imaging sensing techniques might overcome such aforementioned
114 problems. Terrestrial laser scanner systems have shown to be a suitable tool for estimation of sediment
115 redistribution and erosion processes (Nasermoaddeli and Pasche, 2008; Afana et al., 2010; Eltner et al.,
116 2016a; Eltner et al., 2016b; Longoni et al., 2016). However, they are expensive and labour-intensive. A
117 continuous, automated monitoring of many mound areas in parallel is for this reason not possible. An already
118 applied low-cost (up to 5000 USD) topographic monitoring technique is time-lapse photogrammetry which can
119 be applied at variable observation distances and scales (e.g. (James and Robson, 2014; Galland et al., 2016;
120 Eltner et al., 2017; MALLALIEU et al., 2017; Kromer et al., 2019; Blanch et al., 2021). For this technique, the
121 surface has to be monitored under various angles for which several devices are needed to be installed in the
122 field. The Time-of-Flight (ToF) technology offers here a new possibility for surface monitoring, as a technique
123 for a cost-effective high-resolution monitoring of sediment redistribution (Eitel et al., 2011; Hänsel et al., 2016)
124 which can be achieved by a simple installation of one device in the field is missing. ToF-based cameras
125 illuminate the targeted object with a light source for a known amount of time and then estimate the distance

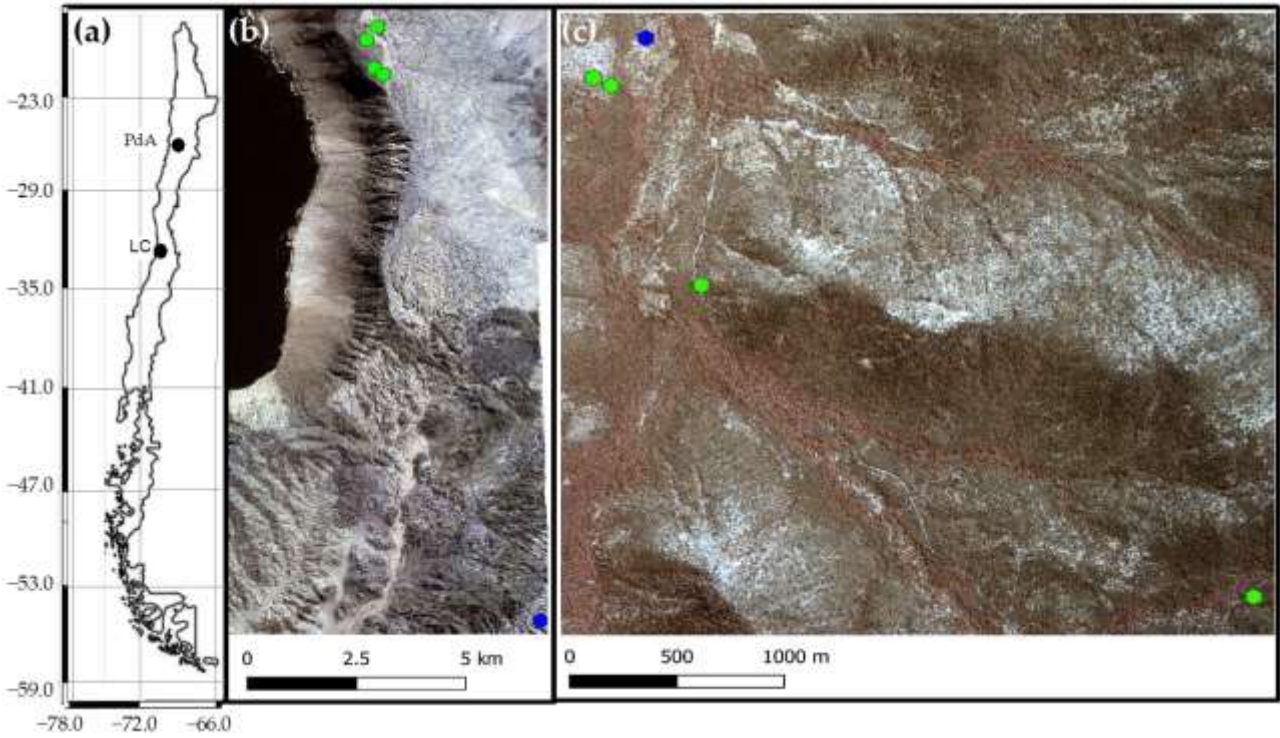
126 between the camera and the object by measuring the time needed for the reflected light to reach the camera
127 sensor (Sarbolandi et al., 2018).

128 In our study we developed, tested and applied a cost-effective Time-of-Flight camera for automated
129 monitoring of the rainfall and animal-driven sediment redistribution in areas affected by burrowing animals with
130 high temporal (four times a day) and spatial (6 mm) resolution. For this, we equipped several plots in remote
131 study sites in the Chilean arid and mediterranean climate zone. We selected these sites in order to analyse
132 sediment redistribution by burrowing activity of vertebrates under different rainfall regimes and as these sites
133 have been shown to be particularly strongly affected by burrowing activity (Grigusova et al., 2021). We
134 estimated the burrowing intensity and its dependence on rainfall. Then, we quantified the daily sediment
135 redistribution within areas affected and not affected by burrowing animals. We analysed the impacts of animal
136 burrowing activity and rainfall on the sediment redistribution and quantified the volume of sediment which is
137 additionally incorporated to the hillslope sediment flux due to the presence of burrows. Finally, we estimated
138 sediment redistribution on a burrow scale and upscaled sediment redistribution rates to the entire hillslopes.
139

140 2. Study sites

141 Our study sites were located in the Chilean Coastal Cordillera in two climate zones (Fig. 1): in the National
142 Park Pan de Azúcar (further as Pan de Azúcar or PdA) and the National Park La Campana (further as La
143 Campana or LC). The Las Lomas site in PdA is located in the arid climate zone of the Atacama Desert with a
144 precipitation rate of 12 mm year⁻¹, and it has a mean annual temperature of 16.8 °C (Übernicket et al., 2021b).
145 Here, the vegetation cover is below 5%, and it is dominated by small desert shrubs, several species of cacti
146 (*Eulychnia breviflora*, *Copiapoa atacamensis*) and biocrusts (Lehnert et al., 2018). LC is located in the
147 mediterranean climate zone with a precipitation rate of 367 mm year⁻¹ and a mean annual temperature of
148 14.1 °C (Übernicket et al., 2021b). LC is dominated by an evergreen sclerophyllous forest with endemic palm
149 trees, *Jubaea chilensis*. Both research sites have a granitic rock base, and the dominating soil texture is sandy
150 loam (Bernhard et al., 2018). In PdA, the study setup consisted of one north-facing and one south-facing
151 hillslope. The hillslope inclinations were ~20°, and a climate station was located ~15 km from the camera sites.
152 In LC, the setup consisted of two north-facing and one south-facing hillslopes. The hillslope inclinations were
153 ~25°, and a climate station was located ~250 m from the south-facing hillslope (Übernicket et al., 2021b).
154 Among the most common vertebrate burrowing animals are in PdA carnivores (*Lycalopex culpaeus*, *Lycalopex*
155 *griseus*); marsupials and rodents (*Phyllotis xanthopygus*, *Phyllotis limatus*, *Abrothrix andinus*) (Jimenez et al.,
156 1992; Cerqueira, 1985) and in LC rodents (*Octodon degus*, *Rattus norvegicus* and *Phyllotis darwini*) and
157 carnivores (*Lycalopex griseus*) (Muñoz-Pedreros et al., 2018)

158



159
 160 **Figure 1.** Location of the cameras and climate stations on which this study was based. Black points show the
 161 location of the research sites in Chile. The green points represent the camera plots, and the blue points the
 162 climate stations: (a) Location of study sites in Chile: PdA stands for Pan de Azúcar, LC for La Campana; (b)
 163 Study setup in Pan de Azúcar; (c) Study setup in LC. The background images in (b) and (c) are orthophotos
 164 created from WorldView-2 data from 19 July 2019. For exact latitude and longitude see Table A2.

165
 166 **3. Methodology**

167 **3.1 Time-of-Flight (ToF) principle**

168 A Time-of-Flight-based camera illuminates an object with a light source, usually in a non-visible
 169 spectrum, such as near-infrared, for a precise length of time. ToF cameras rely on the principle of measuring
 170 the phase shift, with different options to modulate the light source to be able to measure the phase shift. The
 171 here employed cameras used pulse-based modulation, meaning the light pulse was first emitted by the
 172 camera, then reflected from the surface, and finally measured by the camera using two temporary windows.
 173 The opening of the first window is synchronized with the pulse emission i.e. the receiver opens the window
 174 with the same Δt as the emitted pulse. Then, the second window is opened, for the same duration Δt , which is
 175 synchronised with the closing of the first window. The first temporary window thus measures the incoming
 176 reflected light while the light pulse is also still emitting from the camera. The second temporary window
 177 measures the incoming reflected light when no pulse is emitting from the camera. The captured photon number
 178 (i.e. measured by electrical charge) in both windows can be related according to equation 1 and the distance
 179 from the camera to the object can then be calculated as follows:

$$180 \quad d = \frac{1}{2} * c * t * \left(\frac{g_1}{g_1 + g_2} \right) \quad . \quad (1)$$

181 In Eq. (1), d (m) is the distance from the camera to the object, c (m s^{-1}) is the speed of light ($299,792,458 \text{ m s}^{-1}$),
 182 t (s) is the overall time of the illumination and measurement, g_1 is the ratio of the reflected photons to all
 183 photons accumulated in the first window, and g_2 the ratio of the reflected photons to all photons accumulated
 184 in the second window (Sarbolandi et al., 2018; Li, 2014).

185 The sensor in our camera came from Texas Instruments and the data scan contained information on
 186 320 x 240 points. The camera field of view (FOV) and the spatial resolution of the scans depended on the
 187 height of the camera above the surface and camera orientation. The distance was calculated for every point,
 188 and the object was saved in binary format as a collection of 3D points with x-, y- and z-coordinates. The point
 189 clouds taken by the camera were transformed from the binary format to an ASCII format. Each point in the
 190 point cloud was assigned to an x-, y- and z-coordinate. The coordinates were distributed within a three-
 191 dimensional Euclidian space, with the point at the camera nadir (the centre of the camera sensor) being the
 192 point of origin of the 3D Cartesian coordinate system. x- and y-coordinates describe the distance to the point
 193 of origin (m). z-coordinate describes the distance (m) from the object to the camera. The lowest point of the
 194 scanned surface thus has the highest z-coordinate value.

195

196 3.2 Data processing

197 The distortion caused by the hillslope and the camera angle was corrected for each point cloud as
 198 follows:

$$199 z_{cor} = z_{uncor} - \tan(\alpha + \beta) * (y_1 - y_i) \quad . \quad (2)$$

200 In Eq. (2), z_{cor} is the corrected distance (m) between the camera and surface (m), z_{uncor} is the uncorrected z-
 201 coordinate (m), α is the tilt angle of the camera ($^{\circ}$), β is the surface inclination ($^{\circ}$), and y_i (m) is the distance
 202 between each point, and the point with i) an y-coordinate = 0 and ii) the same x-coordinate as the respective
 203 point. The most frequent errors were identified and treated as follows. Due to the ambient light reaching the
 204 camera sensor, the z-coordinate values of some of the points were incorrect (scattering error). To remove this
 205 error, a threshold value was calculated for each point cloud:

$$206 \Omega = mean_{z_{cor}-coordinates} \pm sd_{z_{cor}-coordinates} \quad . \quad (3)$$

207 In Eq. (3), Ω is the threshold value, $mean_{z_{cor}-coordinate}$ is the average value, and $sd_{z_{cor}-coordinate}$ is the standard
 208 deviation of the corrected z-coordinates (m). Then, all points with a z-coordinate above and below this value
 209 were deleted. Point clouds with more than 50% of points above the threshold value Ω were also not considered
 210 for further processing. A drift error occurred when the z-coordinate values of around one-third of the point
 211 clouds decreased by several centimetres from one point cloud to another. Here, the average z-coordinate of
 212 ten point clouds before and after the drift were calculated, and the difference was added to z-coordinates of
 213 the points affected by the drift. The corrected height values were then transformed into a digital surface model
 214 (DSM).

215

216 3.3 Accuracy of the ToF cameras

217 The accuracy of the ToF camera was tested under laboratory conditions by recreating similar surface
 218 conditions as in the field (sloping surface, covered by sediment). An artificial mound using sediment extracted
 219 from a riverbank in central Germany was used, mimicking a mound created by a burrowing animal. During the
 220 test, the camera was installed 100 cm above the surface. The camera FOV was 3 m² and the scan spatial
 221 resolution was 6 mm. The surface was scanned twice by the ToF camera. Then 100 – 450 cm³ of sediment
 222 was manually extracted from the mound. The volume of the extracted sediment was measured by a measuring
 223 cup. After extraction, the surface was again scanned twice by the camera. The experiment was repeated 45
 224 times with varying amounts of extracted sediment. The scans were transformed to point clouds in VoxelViewer-
 225 0.9.10, and the point clouds were corrected according to Eq. (2) and (3). The z-coordinates of the two point
 226 clouds before and two point clouds after the extraction were averaged. The standard deviation of the z-

227 coordinate of the two scans was 0.06 cm. Figure A1 shows the spatially distributed standard deviation. The
 228 deviation increases from the centre towards the corners of the scan. The mound was outlined and only the
 229 points representing the mound were used in the further analysis. The point clouds were then transformed into
 230 DSMs, and the differences between the time steps were calculated. A scan was taken of a smooth surface
 231 (linoleum floor) and a point cloud was created from the data. Then, we fitted a plane into the point cloud and
 232 calculated the distance between the plane and the camera sensor. The standard variation (0.17 cm) in the
 233 distance measurements was saved. Solely, the differences between the DSMs below this variation were
 234 considered in the calculation of the detected sediment extraction. The detected extracted sediment volume
 235 was then calculated for each experiment as follows:

$$236 \text{Vol}_{detected} = \sum_p^1 (DSM_{before} - DSM_{after}) * res^2 \quad , \quad (4)$$

237 In Eq. (4), $\text{Vol}_{detected}$ is the volume of the extracted sediment as detected by the camera (cm^3), p is the number
 238 of pixels, DSM_{before} (cm) is the DSM calculated from the scan taken before the extraction, DSM_{after} (cm) is the
 239 DSM calculated from the scan taken after the extraction, res (cm) is the resolution of the scan, which was 0.6
 240 cm. To evaluate the camera's accuracy, the measured volume of the extracted sediment was compared to the
 241 volume detected by the camera. The camera's accuracy was estimated between the detected volume and
 242 measured volume as follows:

$$243 MAE = \sum_1^n \frac{(\text{Vol}_{detected} - \text{Vol}_{measured})}{area} \quad . \quad (5)$$

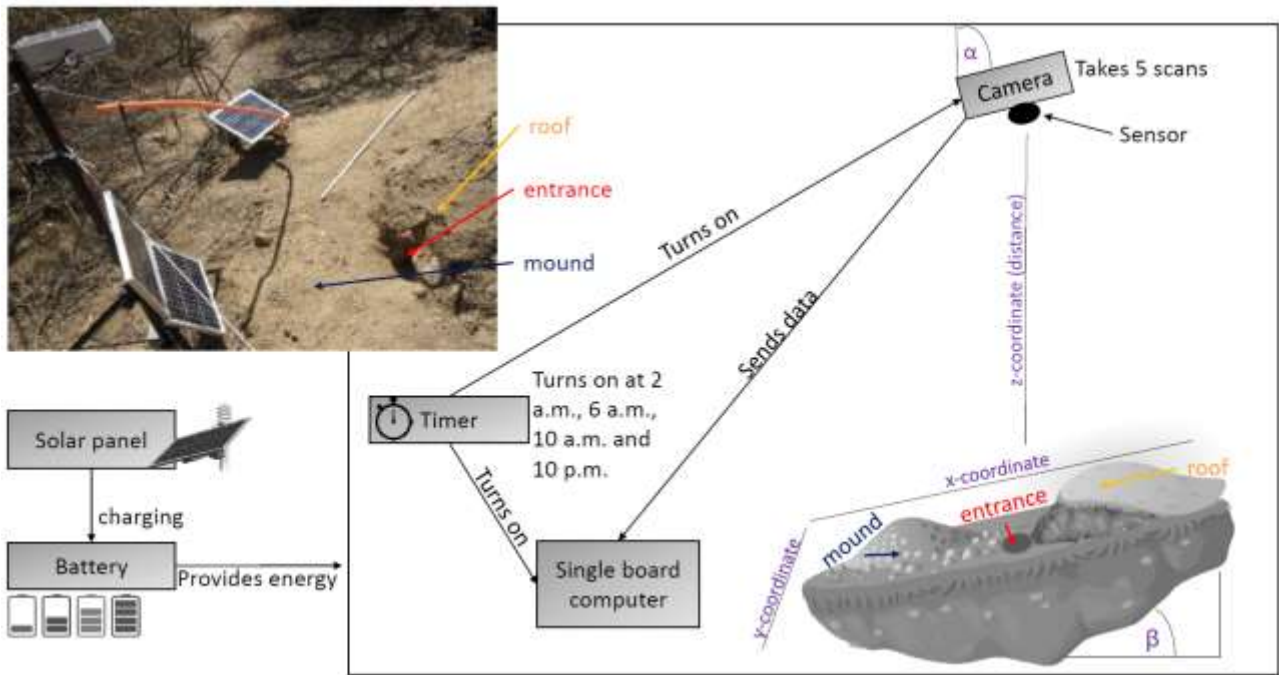
244 In Eq. (5), MAE (cm^3/cm^2) is the mean absolute error, n is the number of scans, $\text{Vol}_{measured}$ (cm^3) is the volume
 245 of the extracted sediment measured by the measuring cup, and the area is the total surface area monitored
 246 by the camera (cm^2).

247

248 3.4 Installation of the cameras in the field

249 We installed 8 custom-tailored ToF-based cameras on 4 hillslopes in two climate zones in areas
 250 including visible signs of bioturbation activity (burrows) and areas without visible signs of bioturbation (Fig. 2).
 251 The cameras were installed in LC on the north-facing upper hillslope (LC-NU), north-facing lower hillslope (LC-
 252 NL), south-facing upper hillslope (LC-SU) and the south-facing lower hillslope (LC-SL); in PdA on the north-
 253 facing upper hillslope (PdA-NU), north-facing lower hillslope (PdA-NL), south-facing upper hillslope (PdA-SU)
 254 and south-facing lower hillslope (PdA-SL). The custom-tailored cameras were installed during a field campaign
 255 in March 2019, the monitoring took place for seven months, and the data were collected in October 2019. The
 256 construction consisted of a 3D ToF-based sensor from Texas Instruments (Li, 2014), a RaspberryPi single board
 257 computer (SBC), a timer, a 12 V 12 Ah battery and three 20 W solar panels for unattended operation (Fig. 2).
 258 Solar panels were located at the camera pole and were recharging the battery via a charge controller. The
 259 camera was located approximately one meter above the surface, facing the surface with a tilt angle of 10
 260 degrees. The timer was set to close the electric circuit 4 times a day: at 1 a.m., 5 a.m., 8 a.m. and 10 p.m. At
 261 these times, the camera and the computer were turned on for 15 minutes. The camera turned on and took five
 262 scans delayed one second from each other and sent them to the SBC. Each camera had its own WiFi (Wireless
 263 Fidelity) and the data could be read from the SBC via Secure Shell (SSH). The cameras collected the data for
 264 the time period of 7 months.

265



266
 267 **Figure 2.** Scheme and photo example of a Time-of-Flight-based camera installation in the field. The photo
 268 example is from upper north-facing hillslope in La Campana. Black boxes describe single installation parts.
 269 Purple descriptions are the variables needed for the correction of the scans. Roof, entrance and mound
 270 describe areas affected by the burrowing animal. The x-, y- and z-coordinates are 3D coordinates identifying
 271 the position of each point in space, where the x-coordinate is the length, y-coordinate is the width and the z-
 272 coordinate is the distance between the camera sensor and the surface. α is the inclination of the camera, and
 273 β is the surface inclination.

274
 275 **3.5 Delineation of the area affected and not-affected by burrowing animals**

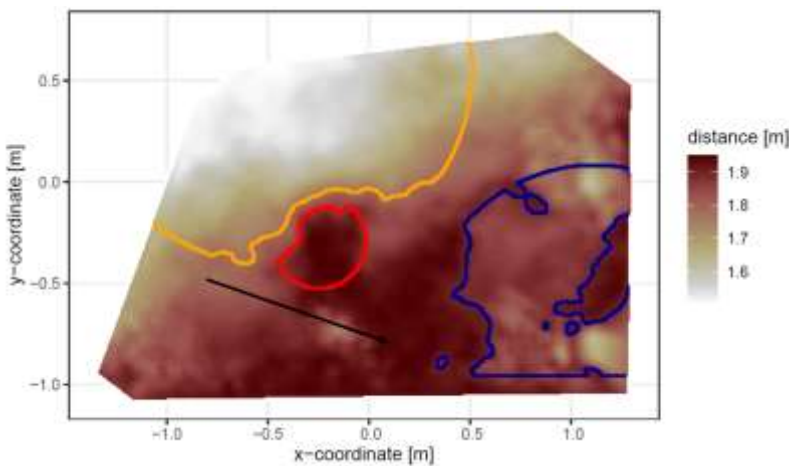
276 The surface area scanned by the cameras was divided by a delineation scheme into areas affected
 277 (A) and not (directly) affected (N) by burrowing animals. The affected areas included three sub-areas: (i) mound
 278 (M), (ii) entrance (E) and (iii) burrow roof (R). “Mound” describes the sediment excavated by the animal while
 279 digging the burrow. “Entrance” describes the entry to the animal burrow up to the depth possible to obtain via
 280 the camera. “Burrow roof” describes the part of the sediment above and uphill the burrow entrance
 281 (BANCROFT et al., 2004). During the burrow’s creation, sediment was not only excavated but also pushed
 282 aside and uphill the entrance, which created the burrow roof. We assume that this elevated microtopographical
 283 feature then forms an obstacle for sediment transported from uphill, which leads to its accumulation in this
 284 area. The remaining surface within the camera’s FOV was classified as not affected (N) by the burrowing
 285 animal during the creation of its burrow.

286 For the delineation, we used the DSM calculated from the point cloud, and a slope layer calculated
 287 from the DSM (Horn, 1981). The DSM had a size of 4 m² a resolution of 0.6 cm. Entrance was assigned to an
 288 area determined by a search algorithm starting at the lowest point of the DSM (pixel with the highest z-
 289 coordinate value). We increased the circular buffer around the starting point by one pixel until the average
 290 depth of the new buffer points was not higher than the height of the camera above the surface, or until the
 291 slope of at least 50% of the new buffer points was not 0. Then, we masked all pixels within the buffer with a
 292 depth lower than the average depth of the points within the buffer, which had a slope that was 0. The remaining
 293 pixels belonged to the entrance area. Then, the surface scan was divided into an uphill and downhill part with

294 regards to the entrance position. Both the uphill and the downhill parts were subdivided into 16 squares, so
 295 that each of the four quadrants within the 2D grid (x- and y-axis) contained four squares. The squares had size
 296 of 0.5 m².

297 To delineate the mound in the downhill part, we first identified the highest points (pixel with the lowest z-
 298 coordinate value) within all 16 squares. We then calculated the distance of these maxima to the entrance, and
 299 the pixel located nearest to the entrance was identified as the highest point of the mound (i.e., seed point).
 300 Consecutively, we increased the circular buffer around the seed point by one pixel until the average depth of
 301 the new buffer points was not lower than the height of the camera above the surface, or until the slope of at
 302 least 50% of the new buffer points was not 0. Then, we masked all pixels within the buffer with a depth higher
 303 than the average depth of the points within the buffer, which had a slope that was 0. The remaining pixels were
 304 classified as mound area. To delineate burrow roof, we used the same approach as for the delineation of
 305 mound and applied it on the uphill part of the surface scan. We used the DEM and slope layers for the
 306 delineation for several reasons. The distance from the surface to the camera was the most important parameter
 307 to derive (i) the deepest point of the entrance and (ii) the highest point of the mound or burrow roof, as this
 308 was (mostly) the closest point to the camera. After the angle correction of the z-coordinate according to chapter
 309 3.2., the surface inclination of the areas without burrow was 0°, while the angle between the border of the
 310 burrow entrance or mound and the not-affected surface was above 0°. Because neither the entrance nor the
 311 mound have a perfect circular form, we would largely overestimate or underestimate the entrance or mound
 312 size. Overestimate by not stopping the search algorithm until the angle between all new points of the buffer to
 313 the rest of the buffer was 0°. Underestimate by stopping the algorithm when the angle of one point of the buffer
 314 to the nearest point of the buffer was 0°. The value of 50% thus minimized the error. All pixels that were not
 315 classified during the entire delineation process were treated as areas not affected by animals. Please note that
 316 the areas termed “not affected” by the burrowing animals are areas adjacent to burrows. This does not imply
 317 complete absence of animals, just no active burrowing.

318 The position and the boundaries of entrance, mound and burrow roof were validated visually (Fig. 3 and A2).



319
 320 **Figure 3.** Corrected digital surface model of the camera on the upper north-facing hillslope in La Campana
 321 with delineated areas. The point of origin of the coordinate system is at the camera nadir. Distance refers to
 322 the distance between surface and camera. The red line delineates the burrow entrance, blue the mound and
 323 orange the burrow roof. The area which was outside of any delineated area was classified as not affected by
 324 animal burrowing activity. The arrow indicates a downhill direction of the hillslope.
 325

326 In LC, the areas affected by the burrowing animal always consisted of an entrance, mound and burrow
327 roof. In PdA, there was no burrow roof on the upper hillslopes. Burrows without a burrow roof were located on
328 shallower parts of the hillslopes (up to an inclination of 5°), and the angle of the burrow entrance to the ground
329 was $\sim 90^\circ$. Burrows with a burrow roof were located on steeper parts of the hillslopes (with an inclination above
330 5°), and the angle of the burrow entrance to the ground was $\sim 45^\circ$.

331

332 **3.6 Calculation of animal-caused and rainfall-caused sediment redistribution**

333 The animal-caused sediment redistribution occurred when the animal actively reworked sediment
334 within its burrow. Under the assumption that the burrows are actively used by the animals, we defined four
335 cases when the sediment was redistributed due to the burrowing activity. For this, we pairwise compared the
336 DSMs of each scan with the scan saved before. The four cases were: (i) as the animal excavates sediment
337 from the entrance, the depth of the entrance must increase in the second scan; (ii) as the excavated sediment
338 accumulates on the mound, the height of the mound must increase in the second scan; (iii) as the burrowing
339 might lead to an expansion or a collapse of the burrow roof, an increase or decrease of the burrow roof must
340 occur between the scans; (iv) as the animal only digs within his burrow, no changes must occur between the
341 two scans within the area not affected by the animal. The animal-caused redistribution was then calculated for
342 these days as the volume of sediment redistributed within mound and burrow roof. The entrance was ignored
343 in the calculation. As the sediment excavated from the entrance accumulated on the mound and the sediment
344 accumulated within entrance collapsed from the burrow roof, by including the entrance in the calculation, these
345 sediment volumes would be counted twice.

346 The rainfall-caused sediment redistribution was calculated as follows: From the data from the climate stations
347 (Übernicker et al., 2021b), we calculated the daily precipitation in mm. The sediment redistribution recorded
348 immediately and within five scans before and after a rainfall event is defined to be the result of the rainfall
349 event. This was necessary as the climate stations are located up to a 15 km distance from the cameras (Fig.
350 1). If both animal-caused and rainfall-caused sediment redistribution took place, the following conditions
351 applied: i) rainfall event occurred, ii) burrow size changed, iii) sediment eroded from not affected areas. Here,
352 the animal-caused sediment redistribution was calculated as the sediment volume excavated from the
353 entrance. The rainfall-caused sediment redistribution was calculated as the sediment volume which eroded
354 from the burrow roof and mound. To this sediment, we added the animal-caused redistributed sediment
355 volume, as this sediment accumulates on the mound.

356 We calculated the rainfall-caused sediment redistribution within (i) areas affected by the burrowing animal (i.e.,
357 entrance, mound and burrow roof) and (ii) within areas not affected by the burrowing animal. To estimate the
358 sediment volume which accumulated within the entrance, we also calculated the volume of redistributed
359 sediment solely (iii) within the entrance.

360

361 **3.7 Calculation of daily sediment mass balance budget**

362 The volume of the redistributed sediment was calculated daily and was then cumulated from the first
363 day of monitoring. For the calculation of the daily sediment redistribution, the change in the surface level
364 detected by the camera was calculated first. For each day, the scans from the day before and after the
365 respective day were averaged and subtracted. The average standard deviation of the z-coordinate of these
366 scans was 0.06 cm. As described in Section 2.2., all values with a difference below and above the threshold

367 value of 0.2 cm were set to 0. The redistributed sediment volume was then calculated from the surface change
368 for each pixel as follows:

$$369 \text{Vol}_{redistributed} = (S_b - S_a) * res^2 \quad . \quad (6)$$

370 In Eq. (6), $\text{Vol}_{redistributed}$ ($\text{cm}^3 \text{ pixel}^{-1}$) is the volume of the calculated redistributed sediment, S_b (cm) the scan
371 before, S_a (cm) the scan after the rainfall event and res is the spatial resolution (cm). Using the daily volume
372 of the redistributed sediment per pixel, we calculated the daily mass balance budget by summing the volume
373 of sediment eroding or accumulating within each delineated area.

374

375 **3.8 Calculation of the overall volume of redistributed sediment after the period of 7 months**

376 From the camera data, we calculated the average cumulative volume of redistributed sediment for the
377 period of 7 months within affected ($\text{Vol}_{affected}$ ($\text{cm}^3 \text{ cm}^{-2} \text{ year}^{-1}$)) and non-affected ($\text{Vol}_{not\ affected}$ ($\text{cm}^3 \text{ cm}^{-2} \text{ year}^{-1}$))
378 areas and the average sediment volume redistributed (excavated) by the animal (Vol_{exc} ($\text{cm}^3 \text{ cm}^{-2} \text{ year}^{-1}$)),
379 separately for each site. We estimated the volume of sediment that was redistributed during rainfall events
380 due to the presence of the burrow (Vol_{add} ($\text{cm}^3 \text{ cm}^{-2} \text{ year}^{-1}$)). Vol_{add} was calculated as the difference in the
381 redistributed sediment volume between affected and non-affected areas according to Eq. (7).

$$382 \text{Vol}_{add} = (\text{Vol}_{affected} - \text{Vol}_{unaffected}) * 1.71 \quad , \quad (7)$$

383 Additionally, we calculated the average volume of the redistributed sediment per burrow ($\text{Vol}_{per\ burrow}$ [cm^3
384 $\text{burrow}^{-1} \text{ year}^{-1}$]).

$$385 \text{Vol}_{per\ burrow} = (\text{Area}_{burrow} * \text{Vol}) * 1.71 \quad (8)$$

386 In Eq. (8), Area_{burrow} (cm^2) is the average size of the burrows that are monitored by the cameras; Vol is $\text{Vol}_{affected}$
387 ($\text{cm}^3 \text{ cm}^{-2} \text{ year}^{-1}$), Vol_{exc} ($\text{cm}^3 \text{ cm}^{-2} \text{ year}^{-1}$) or Vol_{add} ($\text{cm}^3 \text{ cm}^{-2} \text{ year}^{-1}$). Please note that we used the volume of
388 redistributed sediment monitored for 7 months to calculate the volume of sediment per year. We decided to
389 upscale due to several reasons: In contrast to previous studies, our study provides daily data on sediment
390 redistribution which allow a more realistic temporal upscaling than the data sampling with lower frequency. All
391 previous studies estimated the volume of redistributed sediment per year, even though the measurements
392 were conducted less frequently (Table A6, A7 and A8) or even when the measurement was not repeated at all
393 (Übernicket et al., 2021a). These studies thus completely ignored the ongoing sediment excavation and
394 erosion processes. Our study was conducted from middle autumn to middle of spring and thus covered exactly
395 half of the vertebrate burrowing season (Romanach et al. 2005), including dry and wet seasons, thus capturing
396 the key cycles of variability.

397 We then upscaled the $\text{Vol}_{affected}$ ($\text{cm}^3 \text{ cm}^{-2} \text{ year}^{-1}$), Vol_{exc} ($\text{cm}^3 \text{ cm}^{-2} \text{ year}^{-1}$) and Vol_{add} ($\text{cm}^3 \text{ cm}^{-2} \text{ year}^{-1}$)
398 to the hillslope using the same approach. Hillslope-wide upscaling of the results generated in this study was
399 performed by using a previous estimation of vertebrate burrow density (Grigusova et al., 2021). In this study,
400 the density of burrows was measured in situ within eighty 100 m^2 plots and then upscaled to the same hillslopes
401 on which the cameras were located by applying machine-learning methods, using the UAV-data as predictors.
402 Hence, the modelled burrows in the previous study were in fact areas affected by burrowing animals in this
403 study. For upscaling, we applied a random forest model with recursive feature elimination. The model was
404 validated by a repeated Leave-One-Out cross validation. The density of vertebrate burrows was between 6
405 and 12 100 m^2 in LC and between 0 and 12 100 m^{-2} in Pan de Azúcar. Using the hillslope-wide predicted
406 vertebrate burrow densities (Dens_{burrow} (number of burrows 100 m^{-2})) from Grigusova et al. 2021, we estimated
407 the volume of redistributed sediment for each pixel of the raster layers ($\text{Vol}_{per\ pixel}$ ($\text{cm}^3 \text{ m}^{-2} \text{ year}^{-1}$)) according
408 to Eq. (9):

409 $Vol_{per\ pixel} = Vol_{per\ burrow} * Dens_{burrow} * 1.17$ (9)

410 The average hillslope-wide volume of redistributed sediment ($Vol_{hillslope-wide}$ ($m^3\ ha^{-1}\ year^{-1}$)) was then
 411 estimated as follows:

412 $Vol_{hillslope-wide} = \sum_1^m Vol_{per\ pixel} * 0.001 * 1.71$, (10)

413 In Eq (10), m is the number of pixels.

414

415 **4. Results**

416 **4.1 Camera accuracy and data availability**

417 The accuracy between the measured extracted sediment volume and sediment volume calculated
 418 from the camera scans was very high (MAE = $0.023\ cm^3\ cm^{-2}$, $R^2 = 0.77$, SD = $0.02\ cm^3\ cm^{-2}$, Fig. A3). The
 419 accuracy between the calculated and measured extracted sediment was higher when the two scans taken
 420 before as well as after the extraction of the sediment were averaged and the sediment volume was estimated
 421 using these averaged scans. When calculating the redistributed sediment from solely one scan before and
 422 after extraction, the accuracy slightly decreased (MAE = $0.081\ cm^3\ cm^{-2}$, $R^2 = 0.64$). The cameras tended to
 423 overestimate the volume of redistributed sediment. Six out of eight custom-tailored cameras collected data
 424 over the seven-month period (Table A2). One camera collected data for a period of three months and one
 425 camera stopped working a few days after installation. The quantity of usable point clouds taken at 1 a.m., 5
 426 a.m. and 10 p.m. was higher than of point clouds taken at 8 a.m. Approximately 20% of points was removed
 427 from the point clouds before final analysis due to the high scattering at the point cloud corners. After data
 428 filtering (see Section 3.2.), 1326 scans were usable and for 86% of the days, at least one usable scan was
 429 available. The usable scans were distributed continuously within the monitoring period.

430

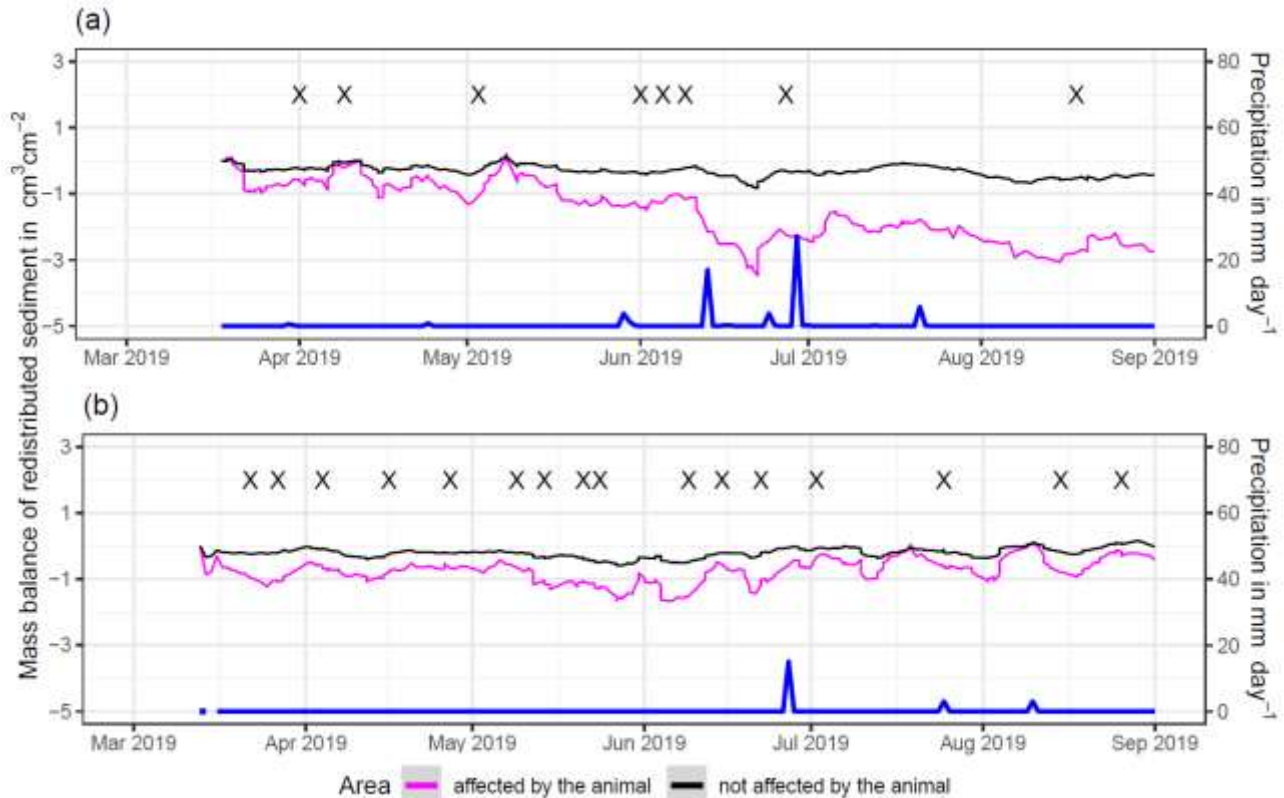
431 **4.3 Mass balance of redistributed sediment**

432 The cameras detected (i) sediment redistribution directly following rainfall events and (ii) due to the
 433 burrowing activity in times without rainfall (Fig. 3, A4 and A5). In all cases, areas affected by burrowing activity
 434 (entrance, burrow roof and mound) exhibited higher sediment redistribution rates than areas not affected by
 435 burrowing. In addition, the volume of redistributed sediment by animal activity was higher after a rainfall event
 436 occurred.

437 In the following, the dynamics are exemplary explained for four cameras. Animal burrowing activity
 438 was detected seven times by the camera LC NU (Fig. 4a, A4, A5) during the monitoring period, by an increase
 439 in sediment volume in the area delineated as mound. Simultaneously, the burrow entrance showed signs of
 440 modification and sediment accumulation, but these changes were less clear. Overall, the volume of the
 441 excavated soil varied. From April until June, up to $0.5\ cm^3\ cm^{-2}$ of sediment was excavated by the animal and
 442 accumulated on the mound. From June until September, animal burrowing activity was detected at four time
 443 slots (5 June 2019, 9 June 2019, 1 July 2019 and 18 August 2019) and sediment volume of up to $2\ cm^3\ cm^{-2}$
 444 accumulated each time on the mound, burrow roof and within the entrance. During the rainfall events of up to
 445 $20\ mm\ day^{-1}$ on 16 June 2019, $27\ mm\ day^{-1}$ on 29 June 2019 and $7\ mm\ day^{-1}$ on 13 July 2019, sediment
 446 volume of up to $4\ cm^3\ cm^{-2}$ eroded, especially from the burrow roof and the mound while a sediment volume
 447 of up to $1\ cm^3\ cm^{-2}$ accumulated within the entrance during each rainfall event. Camera LC-SL (Fig. A4, A5)
 448 showed burrowing activities eight times and sediment volumes of up to $3\ cm^3\ cm^{-2}$ accumulated within the
 449 entrance and burrow roof. The camera detected sediment erosion of up to $2\ cm^3\ cm^{-2}$ after a rainfall event of

450 27 mm day⁻¹ on 27 July 2019. On the south-upper hillslope, the camera detected animal burrowing activity six
451 times, with a sediment accumulation of up to 3 cm³ cm⁻² (Fig. A2 and A3).

452 In contrast, camera PdA-NU pointed to animal burrowing activity up to 15 times where up to 1 cm³ cm⁻²
453 of sediment volume was redistributed from the entrance to the mound (Fig. 4b, A4, A5). At the end of June
454 on 27 June 2019, a rainfall event of 1.5 mm day⁻¹ occurred and up to 2 cm³ cm⁻² of sediment eroded from the
455 burrow roof and accumulated within the burrow entrance. We observed increased sediment redistribution by
456 the animal after the rainfall events. Camera PdA-SL evenly revealed animal burrowing activity up to 15 times
457 ((Fig. A4, A5)). The burrowing had a strong effect on the sediment redistribution. The rainfall event of 1.5 mm
458 day⁻¹ on 27 June 2019 did not cause any detectable surface change.



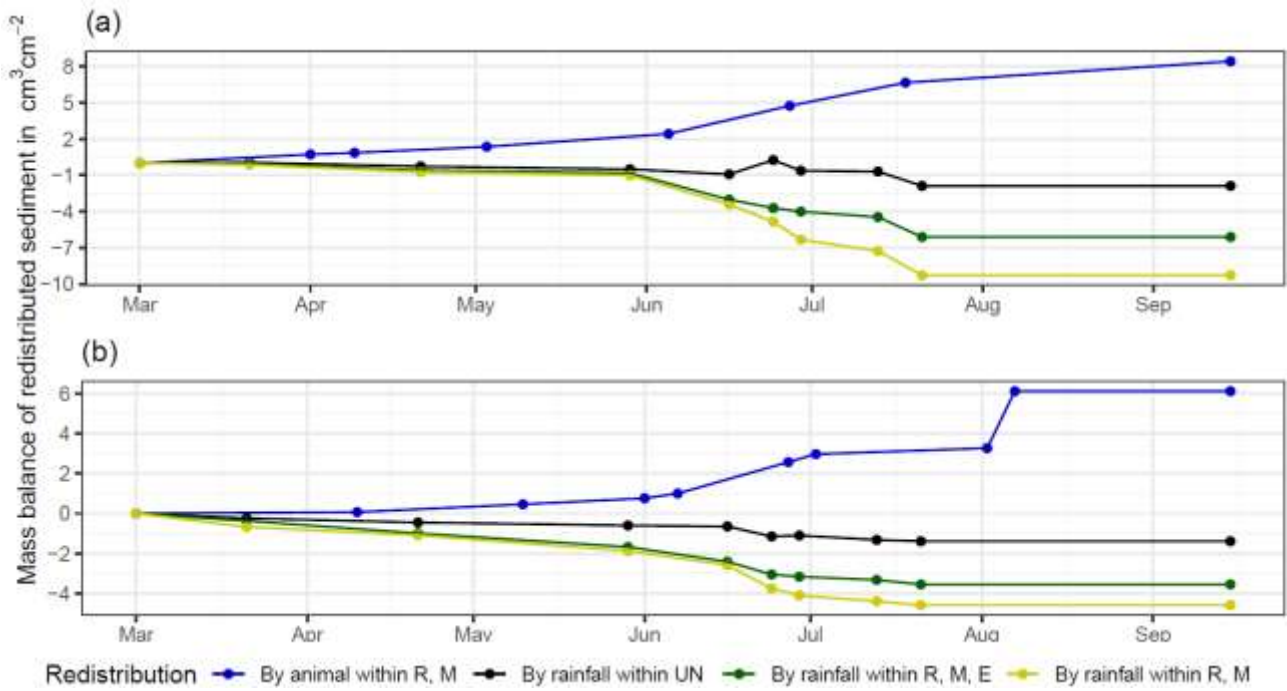
459
460
461 **Figure 4.** Examples of the mass balance of redistributed sediment for areas affected and not affected by
462 burrowing animals: (a) The record of the camera on the upper north-facing hillslope in La Campana showed
463 that larger rainfall events cause a negative sediment balance (sediment loss), followed by a phase of positive
464 sediment mass balance after approximately 3 days due to sediment excavation; (b) The record of the camera
465 on the upper north-facing in Pan de Azúcar hillslope showed a similar pattern to the camera on the upper
466 north-facing hillslope, but the phase of positive mass balance was delayed in comparison. The blue line is the
467 daily precipitation in mm day⁻¹, and "X" marks the days at which animal burrowing activity was detected. Mass
468 balances for all cameras are displayed in Fig. A2 and A3.

469
470 The analysis of cumulative volume of the redistributed sediment caused by burrowing animal activity
471 and rainfall over the monitored period of seven months for all eight cameras showed a heterogeneous pattern.

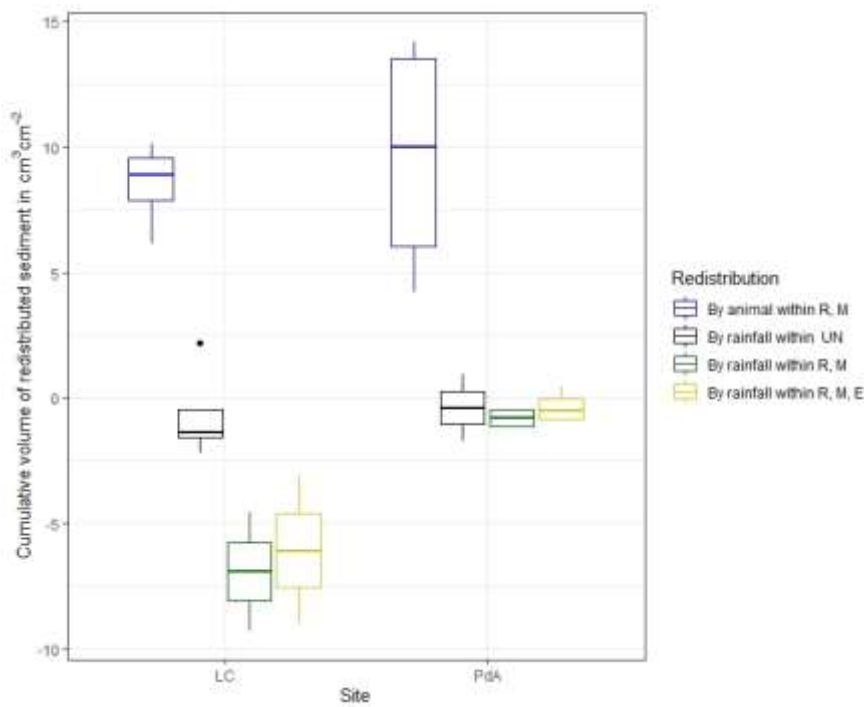
472 In LC, the cumulative volume of the sediment excavated by the animal within the burrow roof and
473 mound increased continuously (Fig. 5, A7). Especially between the rainfall events from June until August, a
474 cumulative volume of on average 6.5 cm³ cm⁻² was excavated by the animal. We calculated that, on average,

475 8.53 cm³ cm⁻² cumulatively eroded from the burrow roof and mound; while 2.44 cm³ cm⁻² sediment volume
 476 accumulated within the entrance (Fig. 5, A7). These results indicate that 28% of sediment eroding from the
 477 burrow roof accumulated within the entrance, while over 62% of sediment eroded downhill. Averaged over all
 478 camera scans, 338% more sediment was redistributed by rain within the affected area compared to the non-
 479 affected area (Fig. 6).

480 In PdA, cameras continuously detected animal burrowing activity and excavation of the sediment (Fig.
 481 A7). The volume of the detected excavated sediment increased steadily within all cameras. The cumulative
 482 sediment accumulation surpasses the sediment eroded due to the rainfall. The volume of the sediment eroded
 483 within the affected areas was 40% higher than within the non-affected areas. The results show that
 484 approximately 50% of the eroded sediment accumulated within the entrance (Fig. 6).
 485



486 Redistribution — By animal within R, M — By rainfall within UN — By rainfall within R, M, E — By rainfall within R, M
 487 **Figure 5.** Examples of the cumulative volume of redistributed sediment within affected and non-affected areas
 488 caused by animal burrowing activity or rainfall in mediterranean La Campana: (a) Upper north-facing hillslope;
 489 (b) Lower south-facing hillslope. Positive values indicate sediment accumulation. Negative values indicate
 490 sediment erosion. E is the burrow entrance; M is the mound; R is burrow roof; UN is the area not directly
 491 affected by the animal burrowing activity. Cumulative volumes for all cameras are in Fig. A7.



492
 493 **Figure 6.** Cumulative volume of the redistributed sediment for all cameras. Positive values indicate sediment
 494 accumulation. Negative values indicate sediment erosion. Whiskers indicate the median of sediment
 495 redistribution. E is the burrow entrance; M the mound; R is the burrow roof; UN is area not affected by the
 496 animal burrowing activity; LC stands for National Park La Campana in the mediterranean climate zone; PdA
 497 stands for National Park PdA in the arid climate zone.

498
 499 **4.4 Volume of redistributed sediment**

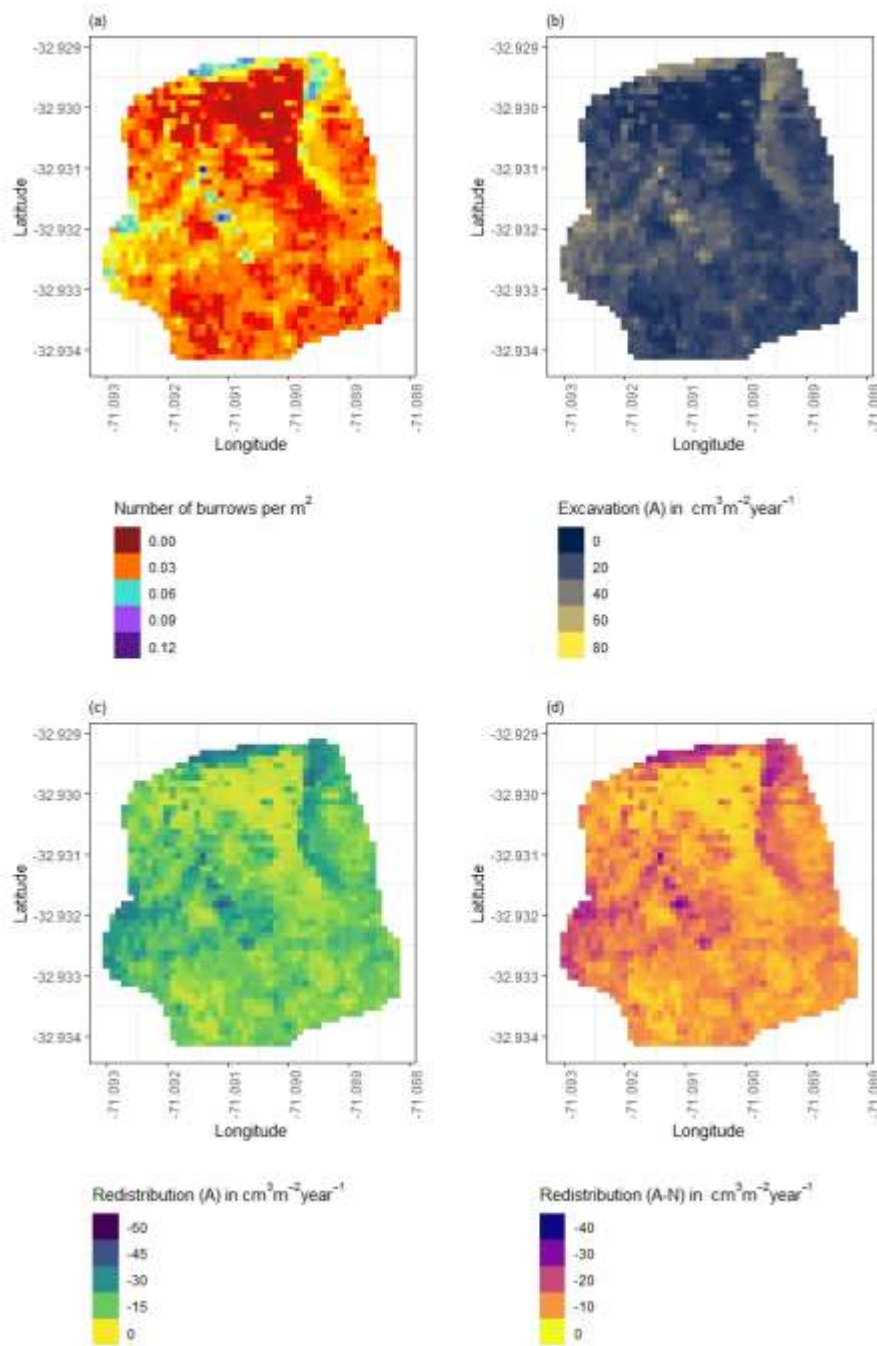
500 The average size of the burrows was 84.36 cm² (SD = 32.54 cm²) in LC and 91.35 cm² in PdA (SD = 8.53
 501 cm²). The animals burrowed on average 1.2 times month⁻¹ in LC and 2.33 times month⁻¹ in PdA. The volume
 502 of the excavated sediment was 102.22 cm³ month⁻¹ in LC and 124.89 cm³ month⁻¹ in PdA. Each time the
 503 animals burrowed, they excavated 42 cm³ sediment volume in LC and 14.33 cm³ sediment volume in PdA.
 504 The burrowing intensity increased in winter after the rainfall occurrences in LC and stayed constant during the
 505 whole monitoring period in PdA. The burrows deteriorate after rainfall events with a rate of 73.03 cm³ month⁻¹
 506 or 63.90 cm³ event⁻¹ in LC and 10.53 cm³ month or 24.57 cm³ event⁻¹.

507 The overall volume of the sediment excavated by the animal and redistributed during rainfall events
 508 varied between the sites (Table 1). The volume of the sediment redistributed by the animal was lower in LC
 509 than in PdA. However, on the hillslope scale, a higher total area-wide volume of excavation was calculated for
 510 LC compared to PdA, due to the higher burrow density in LC. The volume of the sediment redistributed within
 511 the area affected by burrowing activity during rainfall events was higher in LC than in PdA. The volume of
 512 additionally redistributed sediment due to the presence of burrows was higher in LC than in PdA (Table 1, Fig.
 513 7).

514
 515 **Table 1.** Summary of the volume of redistributed sediment, according to area and disturbance type. Vol_{exc}
 516 describes volume of the sediment excavated by the animals. Vol_{affected} describes volume of the sediment
 517 redistributed during rainfall events within affected areas. Vol_{add} describes the difference in redistributed
 518 sediment volume within affected and not affected area during rainfall.

Disturbance	Area	PdA	LC
Vol_{exc}	Affected area	16.41 cm ³ cm ⁻² year ⁻¹	14.62 cm ³ cm ⁻² year ⁻¹
	Per burrow	1498.66 cm ³ burrow ⁻¹ year ⁻¹	1226.61 cm ³ burrow ⁻¹ year ⁻¹
	Hillslope-wide	0.18 m ³ ha ⁻¹ year ⁻¹	0.67 m ³ ha ⁻¹ year ⁻¹
Vol_{affected}	Affected area	-1.97 cm ³ cm ⁻² year ⁻¹	-10.44 cm ³ cm ⁻² year ⁻¹
	Per burrow	-126.36 cm ³ burrow ⁻¹ year ⁻¹	-876.38 cm ³ burrow ⁻¹ year ⁻¹
	Hillslope-wide	-0.05 m ³ ha ⁻¹ year ⁻¹	-0.48 m ³ ha ⁻¹ year ⁻¹
Vol_{add}	Affected area	-1.18 cm ³ cm ⁻² year ⁻¹	-7.37 cm ³ cm ⁻² year ⁻¹
	Per burrow	-48.36 cm ³ burrow ⁻¹ year ⁻¹	-619.2 cm ³ burrow ⁻¹ year ⁻¹
	Hillslope-wide	-0.02 m ³ ha ⁻¹ year ⁻¹	-0.34 m ³ ha ⁻¹ year ⁻¹

519



520
 521 **Figure 7.** Example of the hillslope-wide volume of redistributed sediment for a time period of one year on the
 522 south-facing hillslope in La Campana: (a) Density of burrows as estimated by Grigusova et al. (2021); (b)
 523 Volume of the sediment excavated by the animals; (c) Volume of the sediment redistributed during rainfall
 524 events within affected areas; (d) Volume of additionally redistributed sediment during rainfall events due to the
 525 presence of the burrows. The values were calculated per burrow as stated in Section 3.7. by subtracting the
 526 sediment volume redistributed within animal-affected areas from the sediment volume redistributed within non-
 527 affected area and then upscaled. The letters in brackets indicate if the upscaling was conducted using data
 528 from affected or non-affected areas by burrowing animals. “A” stands for affected area. By “A-N”, the
 529 redistribution calculated from non-affected areas was subtracted from the redistribution calculated within
 530 affected areas to obtain the additional volume of redistributed sediment due to the burrows’ presence.
 531
 532

533 **5. Discussion**

534 Our results showed that the custom-made ToF device is a suitable tool for high-resolution, automated
535 monitoring of surface changes, applicable also in remote areas. The ability of a continuous observation of
536 sediment redistribution over a longer time during our study provided new insights into the importance of
537 burrowing animals for sediment redistribution. Our research reveals that the presence of vertebrate burrows
538 increases hillslope sediment redistribution rates much more than previously assumed (up to 208%). We
539 showed that the quantity of animal-related sediment redistribution, however, varied with rainfall occurrence,
540 with an increase in sediment redistribution between 40% in the arid research area and 338% percent in the
541 mediterranean research area.

542

543 **5.1 Suitability of the ToF method for surface monitoring**

544 The here proposed monitoring technique enables an automatic monitoring of surface changes on a
545 microtopographic scale, and its measurement continuity allows for the analysis of ongoing
546 biogeomorphological processes in high temporal resolution.

547 With regard to the costs, measurement frequency and sampling autonomy, the custom-made ToF
548 device stands in contrast to earlier studies that used laser scanning technology to monitor microtopographic
549 changes (Table A5). Previous studies mainly applied expensive laser scanning for the estimation of sediment
550 redistribution, and the research sites had to be personally revisited for each of the measurements
551 (Nasermoaddeli and Pasche, 2008; Eltner et al., 2016a; Eltner et al., 2016b; Hänsel et al., 2016). The
552 estimated costs in studies using time-lapse photogrammetry were similar to our study (up to 5000 USD) (James
553 and Robson, 2014; Galland et al., 2016; MALLALIEU et al., 2017; Eltner et al., 2017; Kromer et al., 2019;
554 Blanch et al., 2021). However, for time-lapse monitoring, several devices needing different viewing angles
555 increases installation efforts significantly.

556 In terms of data quality, our ToF device is more precise or comparable to those employed in other
557 studies. The accuracy of the camera ($R^2 = 0.77$) was in the range of previous studies ($R^2 = 0.26$ – 0.83 (Eitel et
558 al., 2011), Table A5). The horizontal point spacing of our cameras was 0.32 cm, and the maximum number of
559 points per cm² was 8.5. These values are similar to previous studies in which the used devices had a horizontal
560 point spacing in the range of 0.25–0.57 cm (Kaiser et al., 2014; Nasermoaddeli and Pasche, 2008)) (Table
561 A5), and the maximum number of points per cm² in a range of 1 point–25 points cm⁻² (Eitel et al., 2011; Longoni
562 et al., 2016) (Table A5).

563 Our cameras tended to slightly overestimate or underestimate the volume of redistributed sediment.
564 This error occurs when the pulse reflects from several vertical objects such as walls or, in our case, branches
565 or stones and then enters the camera sensor. This phenomenon was also observed in previous studies
566 applying laser scanners and is inevitable if the goal is to study surface changes under natural field conditions
567 (Kukko and Hyyppä, 2009; Ashcroft et al., 2014). During operation of the cameras, we learnt that our newly
568 developed instruments are particularly capable of delivering usable scans at night. This is likely due to the
569 strong scattered sunlight reaching the camera sensor during the day, blurring the data (Li, 2014). Thus, in
570 future studies, we recommend focusing on nocturnal operation to prevent light contamination from the
571 surroundings.

572 We could thus prove that ToF cameras are a suitable and cost-effective method for a continuous
573 monitoring of sediment redistribution at a microtopographic scale without the need of time, labour and cost
574 intensive laser scanning/time-lapse photogrammetry campaigns.

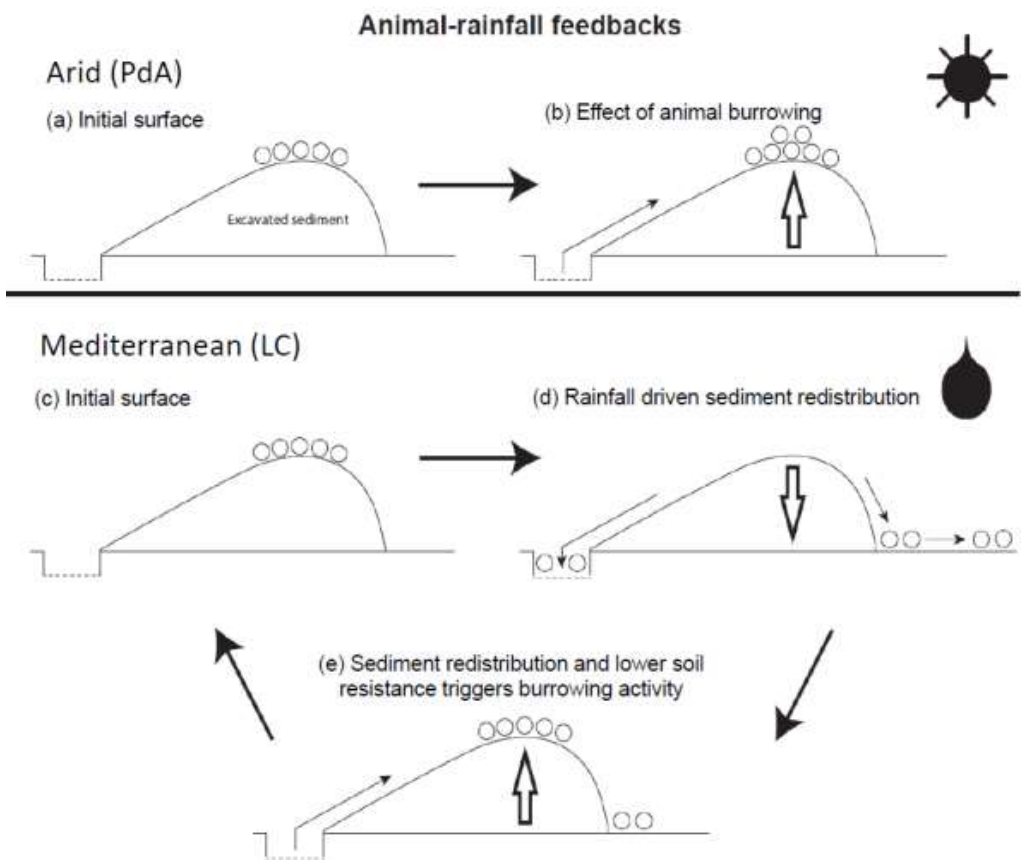
575

576 **5.2. Sediment Redistribution**

577 Our research reveals that the presence of vertebrate burrows generally increases hillslope sediment
578 redistribution. We show, however, that the ratio between the sediment redistribution caused by rainfall in the
579 areas affected and not affected by burrowing animals varies between climate zones. Sediment redistribution
580 in the affected areas was 40% higher at the arid research site, and at the mediterranean research site, it was
581 338% higher when compared to areas not affected by burrowing animals (Table A6).

582 By monitoring microtopographical changes in a high spatio-temporal resolution, we found that the
583 occurrence of larger rainfall events played a two-fold, accelerating role in influencing sediment redistribution
584 (Fig. 5, A4). Firstly, rainfall-runoff eroded burrow material caused increased sediment loss. This was followed
585 by animal burrowing activity after the rainfall. This means that rainfall triggered animal burrowing activity which
586 was very likely related to a lower burrowing resistance of the soil due to the increased soil moisture (Rutin,
587 1996; Romañach et al., 2005; Herbst and Bennett, 2006). This double feedback led to frequently occurring but
588 small redistribution rates. However, cumulatively, the mechanism increased downhill sediment fluxes. Previous
589 studies most likely missed this low magnitude but frequent surface processes due to a lower monitoring
590 duration and frequency, or artificial laboratory conditions, and thus, did not quantify the full volume of
591 redistributed sediment associated with burrowing activity. To quantify all occurred sediment redistribution
592 processes, a continuous surface monitoring, like the here presented, is needed.

593



594

595 **Figure 8.** Scheme of animal-driven and rainfall-driven sediment redistribution processes in both investigated
596 climate zones: (a) Describes the initial surface of the burrow before the start of a sediment redistribution
597 process, and (b) the animal excavation process in the arid climate zone. Here, due to rarely occurring rainfall
598 events, sediment redistribution is mostly controlled by the animal burrowing activity; (c) describes the initial

599 burrow surface in the mediterranean climate zone, (d) the process of sediment redistribution during a rainfall
600 event and (e) the subsequent animal burrowing activity. Burrowing is triggered by decreased soil resistance
601 due to the increased soil moisture after rainfall as well as by sediment accumulation within the burrow's
602 entrance. Burrowing activity leads to a new supply of sediment being excavated to the surface. In the
603 mediterranean climate zone, sediment redistribution is controlled by both animal burrowing activity and rainfall.
604 The alternating excavation and erosion process ultimately lead to an increase in redistribution rates.

605
606 Our results indicate an up to 338% increase in the sediment volume redistributed during rainfall events
607 measured in the areas affected by burrowing animals when compared to not affected areas. In contrast to our
608 result, the maximum increase estimated in previous studies was 208% (Table A6, (Imeson and Kwaad, 1976).
609 The two climate zones also show different patterns: In the mediterranean climate, the contribution of animals'
610 (vertebrates') burrowing activity appear larger than previously observed by using field methods such as erosion
611 pins or splash traps (from -3% until - 208%, Table A6, (Imeson and Kwaad, 1976; Hazelhoff et al., 1981;
612 Black and Montgomery, 1991). In contrast, in arid PdA, our study found a much smaller increase (40%, Table
613 A6) in the sediment volume redistributed during rainfall events measured in the areas affected by burrowing
614 animals when compared to not affected areas. This is lower than previously estimated (125%, Table A6, (Black
615 and Montgomery, 1991). However, solely one rainfall event above 0.2 mm day⁻¹ occurred during our monitoring
616 period. Hence, we conclude that the contribution of burrowing activity of animals to hillslope sediment transport
617 is much larger in areas with frequent rainfall events than previously thought, while it has been realistically
618 estimated by previous studies for areas with rare rainfall events (Table A6).

619 Overall, our study revealed a strong impact of animal excavation processes on sediment redistribution
620 in the mediterranean climate zone (0.67 m³ ha⁻¹ year⁻¹), which were more in a range of excavated volume
621 observed in previous studies by bears and porcupines (0.49 m³ ha⁻¹ year⁻¹, Table A8, (Hall et al., 1999) than
622 rodents (0.02 m³ ha⁻¹ year⁻¹, (Hall et al., 1999). The estimated sediment excavation in the arid climate zone
623 (0.18 m³ ha⁻¹ year⁻¹, Fig. A4, Table A8) was in the order of magnitude of previous studies (0.05–0.2 m³ ha⁻¹
624 year⁻¹, Table A8, (Black and Montgomery, 1991; Yoo et al., 2005). Our results thus suggest that animal
625 burrowing activity is an important part of the environmental mechanisms leading to increased sediment fluxes
626 in wetter (as a consequence of animal-triggered excavation and rainfall-triggered erosion) and drier (as a
627 consequence of animal-triggered excavation) regions (Fig. 5).

628 Magnitudes of sediment volume redistributed within areas affected by burrowing animals similar to our
629 results were previously obtained solely in studies applying rainfall simulators. These studies estimated an
630 increase in the volume of sediment redistributed during rainfall events, measured in the areas affected by
631 burrowing animals when compared to not affected areas, to be between 205% and 473% (Table A6, (Li et al.,
632 2018; Chen et al., 2021). However, a rainfall simulator can only provide data on surface processes within a
633 plot of a few m² in size and under ideal laboratory conditions while ignoring the uphill microtopography,
634 vegetation cover and distribution (Iserloh et al., 2013), which were shown to reduce erosion rates. More
635 importantly, the rainfall intensity on hillslopes decreases with (i) the angle of incidence of the rain, (ii) the
636 inclination of the surface and iii) the relative orientation of the sloping surface to the rain vector (Sharon, 1980).
637 When simulating a rainfall event with the same rainfall volume as in the field, the rain is induced directly over
638 the treated surface and has thus a higher velocity which leads to an increased splash erosion than under
639 natural conditions (Iserloh et al., 2013). We thus propose that the rainfall experiments overestimate the erosion
640 rate while the correct erosion rate can be measured solely under field conditions.

641 Cumulative sediment redistribution within burrow roof, mound and entrance was, on average, 28%
 642 lower than cumulative sediment redistribution only within the mound and the burrow roof (Figure A7). These
 643 results suggest that 28% of the eroded sediment from animal mounds and burrow roofs is re-accumulated
 644 within the burrow entrance during rainfall-runoff events, and the remaining 62% is incorporated into overall
 645 hillslope sediment flux. Our numbers contrast with previous studies, which quantified that about 58% of the
 646 sediment excavated by animals will accumulate back in the burrow entrance and only 42% is incorporated to
 647 downhill sediment flux (Andersen, 1987; Reichman and Seabloom, 2002). Hence, our results indicate not only
 648 higher redistribution rates within areas affected by burrowing animals but also point to much higher supply of
 649 sediment to the downhill sediment flux than previously thought.

650 Our cost-effective ToF device provides data on surface changes in a high spatio-temporal resolution.
 651 The high temporal resolution was able to unravel ongoing low magnitude but frequent animal excavation and
 652 erosion processes. The high spatial resolution enabled us to estimate the exact volume of sediment fluxes
 653 from the burrows downhill. The here presented results indicate that the contribution of burrowing animals on
 654 the burrow as well as on the hillslope scale was much higher than previously assumed. Our results can be
 655 integrated into long-term soil erosion models that rely on soil processes and improve their accuracy by
 656 including animal-induced surface processes on microtopographical scales in their algorithms.

657
 658

659 **Funding:** This study was funded by the German Research Foundation, DFG [grant numbers
 660 BE1780/52-1, LA3521/1-1, FA 925/12-1, BR 1293-18-1], and is part of the DFG Priority Programme
 661 SPP 1803: EarthShape: Earth Surface Shaping by Biota, sub-project “Effects of bioturbation on rates
 662 of vertical and horizontal sediment and nutrient fluxes”.

663 **Institutional Review Board Statement:** Not applicable.

664 **Informed Consent Statement:** Not applicable.

665 **Acknowledgments:** We thank CONAF for the kind support provided during our field campaign.

666 **Competing interests:** There is no conflict of interest.

667 **Author contribution:** JB, AL and SA planned the campaign; PG and SA performed the measurements; PG
 668 analysed the data and wrote the manuscript draft; AL, JB, NF, RB, KÜ, LP, CR, DK and PP reviewed and edited
 669 the manuscript.

670 **Code/Data availability:** Code and all raw data can be provided by the corresponding author upon request.

671

672 **Appendices**

673 **Table A1.** List of abbreviations

α [°]	Tilt angle of the camera
b [°]	Surface inclination
Ω	Threshold value for the scan scattering error
A	Affected area
Affected area	Area directly affected by the burrowing animal
Area_{burrow}	mean in the field measured size of the burrows which are monitored
Area	total surface area monitored by the camera
BD	Bulk density

c [m/s]	Speed of light
D	Distance from the camera to the object
Dens_{burrow}	Burrow density
DSM	Digital surface model
DSM_{after}	DSM calculated from the scan taken after the extraction
DSM_{before}	DSM calculated from the scan taken before the extraction
Entrance	entrance to the animal burrow
g [-]	ratio [-] of the reflected photons to all photons
LC	National Park LC
LC-NL	Camera in LC on the lower north-facing hillslope
LC-NU	Camera in LC on the upper north-facing hillslope
LC-SL	Camera in LC on the lower south-facing hillslope
LC-SU	Camera in LC on the upper south-facing hillslope
MAE	Mean absolute error
MAP [°]	Mean annual precipitation
m.a.s.l.	Meters above sea level
MAT	Mean annual temperature
mClay [%]	Mean content of clay
mean_{z-coordinate}	Mean value of the z-coordinates
Mound	the sediment excavated by the animal while digging the burrow
mSand [%]	Mean content of sand
mSilt [%]	Mean content of silt
N	Number of scans
N	Not affected area
Not affected area	Area not directly affected by the burrowing animal
PdA	National Park Pan de Azúcar
PdA-NL	Camera in PdA on the lower north-facing hillslope
PdA-NU	Camera in PdA on the upper north-facing hillslope
PdA-SL	Camera in PdA on the lower south-facing hillslope
PdA-SU	Camera in PdA on the upper south-facing hillslope
Res	Resolution
Roof	sediment pushed aside and uphill the entrance during burrow creation
S_a	scan after the rainfall event
S_b	scan before the rainfall event
SBC	Single board computer
sd_{z-coordinate}	standard deviation of the z-coordinates
SSH	Secure shell
t [s]	Overall time of camera illumination
TOC [%]	Total organic carbon
ToF	Time-of-Flight

Vol_{affected}	volume of redistributed sediment within affected area
Vol_{detected}	volume of the extracted sediment as detected by the camera
Vol_{add}	difference in redistributed sediment volume between affected and not affected areas
Vol_{exc}	Volume of the sediment excavated by the animal
Vol_{hillslope-wide}	Hillslope-wide volume of redistributed sediment
Vol_{measured}	volume of the extracted sediment measured by the measuring cup
Vol_{per burrow}	Volume of redistributed sediment per burrow
Vol_{per pixel}	Volume of redistributed sediment per pixel
Vol_{redistributed}	volume of the calculated redistributed sediment
Vol_{not affected}	volume of redistributed sediment within not affected area
y_i	distance of the point to the point of origin at the camera nadir
z_{cor}	Corrected z-coordinate
z_{uncor}	Uncorrected z-coordinate

674

675 **Table A2.** Number of usable scans for each camera

Camera	Latitude	Longitude	Number of scans	Percentage of usable scans taken at 1am / 5am / 8am / 10pm	Time period
PdA-NU	-25.98131	-70.6166	238	29 / 27 / 20 / 24	18.3.-18.9.
PdA-NL	-25.98277	-70.61278	52	24 / 0 / 40 / 36	27.3.-31.5
PdA-SU	-25.97477	-70.61641	351	30 / 26 / 32 / 11	16.3.-19.9.
PdA-SL	-25.97177	-70.61409	167	48 / 38 / 7 / 8	16.3.-19.9.
LC-NU	-32.95230	-71.06231	215	37 / 20 / 8 / 33	9.3.-9.9.
LC-NL	-32.93928	-71.08613	3	-	6.3.-12.9
LC-SU	-32.93078	-71.09066	160	22 / 28 / 26 / 25	28.3.-22.5
LC-SL	-32.93110	-71.08987	167	27 / 25 / 22 / 26	16.3.-19.9.

676

677 **Table A3.** Summary of the volume of redistributed sediment, according to area and disturbance type. Vol_{exc}
678 describes volume of the sediment excavated by the animals. Vol_{affected} describes volume of the sediment
679 redistributed during rainfall events within affected areas. Vol_{add} describes the difference in redistributed
680 sediment volume within affected and not affected area during rainfall.

Disturbance	Area	PdA	LC
Vol_{exc}	Affected area	16.41 cm ³ cm ⁻² year ⁻¹	14.62 cm ³ cm ⁻² year ⁻¹
	Per burrow	1498.66 cm ³ burrow ⁻¹ year ⁻¹	1226.61 cm ³ burrow ⁻¹ year ⁻¹
	Hillslope-wide	0.18 m ³ ha ⁻¹ year ⁻¹	0.67 m ³ ha ⁻¹ year ⁻¹
Vol_{affected}	Affected area	-1.97 cm ³ cm ⁻² year ⁻¹	-10.44 cm ³ cm ⁻² year ⁻¹
	Per burrow	-126.36 cm ³ burrow ⁻¹ year ⁻¹	-876.38 cm ³ burrow ⁻¹ year ⁻¹
	Hillslope-wide	-0.05 m ³ ha ⁻¹ year ⁻¹	-0.48 m ³ ha ⁻¹ year ⁻¹
Vol_{add}	Affected area	-1.18 cm ³ cm ⁻² year ⁻¹	-7.37 cm ³ cm ⁻² year ⁻¹

Per burrow	-48.36 cm ³ burrow ⁻¹ year ⁻¹	-619.2 cm ³ burrow ⁻¹ year ⁻¹
Hillslope-wide	-0.02 m ³ ha ⁻¹ year ⁻¹	-0.34 m ³ ha ⁻¹ year ⁻¹

681

682

683 **Table A4.** Summary of the volume of redistributed sediment for the period of 7 months, according to area and
684 disturbance type. Vol_{exc} describes volume of the sediment excavated by the animals. Vol_{affected} describes
685 volume of the sediment redistributed during rainfall events within affected areas. Vol_{add} describes the difference
686 in redistributed sediment volume within affected and not affected area during rainfall.

Disturbance	Area	PdA	LC
Vol_{exc}	Affected area	9.57 cm ³ cm ⁻² 7 months ⁻¹	8.53 cm ³ cm ⁻² 7 months ⁻¹
	Per burrow	874.22 cm ³ burrow ⁻¹ 7 months ⁻¹	715.52 cm ³ burrow ⁻¹ 7 months ⁻¹
	Hillslope-wide	0.11 m ³ ha ⁻¹ 7 months ⁻¹	0.39 m ³ ha ⁻¹ 7 months ⁻¹
Vol_{affected}	Affected area	-1.15 cm ³ cm ⁻² 7 months ⁻¹	-6.09 cm ³ cm ⁻² 7 months ⁻¹
	Per burrow	-73.71 cm ³ burrow ⁻¹ 7 months ⁻¹	-511.22 cm ³ burrow ⁻¹ 7 months ⁻¹
	Hillslope-wide	-0.03 m ³ ha ⁻¹ 7 months ⁻¹	-0.28 m ³ ha ⁻¹ 7 months ⁻¹
Vol_{add}	Affected area	-0.69 cm ³ cm ⁻² 7 months ⁻¹	-4.30 cm ³ cm ⁻² 7 months ⁻¹
	Per burrow	-28.21 cm ³ burrow ⁻¹ 7 months ⁻¹	-361.20 cm ³ burrow ⁻¹ 7 months ⁻¹
	Hillslope-wide	-0.01 m ³ ha ⁻¹ 7 months ⁻¹	-0.2 m ³ ha ⁻¹ 7 months ⁻¹

687

688 **Table A5.** Review of studies which used laser scanners for the estimation of surface processes.

Reference	R ²	Error	Horizontal point spacing	Points per cm ²	Model	Price
Our results	0.77	0.15 cm	0.32 cm	8.5	Texas Instruments OPT3101	900 USD
(Eitel et al., 2011)	0.23- 0.86	0.07 cm	NA	25	Leica ScanStation 2	102 375 USD
(Eltner et al., 2013)	NA	0.4 cm	NA	6.4	Riegl LMS- Z420i	16 795 USD
(Kaiser et al., 2014)	NA	NA	0.57 cm	NA	Riegl LMS- Z420i	16 795 USD
(Longoni et al., 2016)	NA	NA	NA	1	Riegl LMS- Z420i	16 795 USD
(Morris et al., 2011)	NA	0.5 cm	NA	NA	Maptek I-Site 4400LR	240 000 USD
(Nasermoaddeli and Pasche, 2008)	NA	0.2 cm	0.25 cm	NA	Leica Cyrax HDS 2500	4500 USD

(Thomsen et al., 2015)	NA	NA	0.4 cm	NA	Leica ScanStation 2	102 375 USD
------------------------	----	----	--------	----	---------------------	-------------

689

690 **Table A6.** Review of studies which estimated the sediment redistribution in areas affected and not affected
691 areas and the proposed impact.

Reference	Climate	Animals	Method	Monitoring period	Frequency	Affected areas	Not affected areas	Impact
Our results	arid	vertebrates	scanning	7 months	Daily	1.97 cm ³ cm ⁻² year ⁻¹	1.39 cm ³ cm ⁻² year ⁻¹	+40 %
Our results	Mediterranean	vertebrates	scanning	7 months	daily	10.44 cm ³ cm ⁻² year ⁻¹	1.39 cm ³ cm ⁻² year ⁻¹	+338 %
(Imeson and Kwaad, 1976)	continental	rodents	erosion pins	15 months	monthly	20 mm		NA
(Imeson and Kwaad, 1976)	continental	rodents	splash boards	15 months	monthly	91.75g 24.49 cm ⁻² = 3.75 cm ³ cm ⁻²	94g	-3%
(Imeson and Kwaad, 1976)	continental	rodents	rainfall simulation (7.5 cm / hour intensity)	One-time measurement	NA	0.2 g – 0.73 g	0.009 g – 0.23 g	+208 %
(Imeson, 1977)	continental	vertebrates	rainfall simulation	One-time measurement	NA	0.18-0.3 100 J ⁻¹ m ⁻² rain	0.146 100 J ⁻¹ m ⁻² rain	+123 %
(Hazelhoff et al., 1981)	continental	earthworms	splash traps	12 months	monthly	NA	NA	+180 %
(Black and Montgomery, 1991)	arid	pocket gopher	erosion pins	10 months	2 months	NA	NA	+125 %
(Hakonson, 1999)	temperate	pocket gophers	rainfall simulation	2 years	2 – 3 weeks	2.4 – 8.7 mg ha ⁻¹	4.4 – 15 mg ha ⁻¹	-43%

			r (60 mm / hour)							
(Li et al., 2018)	temperate	mole crickets	rainfall simulation (36 mm / hour)	One time measurement	15	22.1 g cm ⁻² = 5.2 cm ³ cm ⁻²	115	5 g cm ⁻² = 1.09 cm ³ cm ⁻²	123	+473 %
(Li et al., 2018)	temperate	mole crickets	rainfall simulation (36 mm / hour)	One time measurement	15	35.3 g cm ⁻² = 6.24 cm ³ cm ⁻²		5 g cm ⁻² = 1.09 cm ³ cm ⁻²	123	+473 %
(Chen et al., 2021)	lab	chinese zocor	rainfall simulation (80 mm / hour)	One-time measurement	3	2,69 g cm ⁻² = 2.69 cm ³ cm ⁻²		0,88 g cm ⁻² = 0.88 cm ³ cm ⁻²		+205 %

692

693

694 **Table A7.** Review of studies which estimated the sediment redistribution in areas affected by burrowing
695 animals, average burrow density as found in the literature and area-wide yearly contribution of burrowing
696 animals to sediment redistribution.

Climate	Animals	Affected areas	Average burrow density	Average burrow size	Area-wide redistribution
Arid	vertebrates	1.97 cm ³ cm ⁻² year ⁻¹	0-12 10 m ⁻² = 0-1.2 m ⁻² (Grigusova et al., 2021)	91.35 cm ²	1.18 cm ³ ha ⁻² year ⁻¹
mediterranean	vertebrates	10.44 cm ³ cm ⁻² year ⁻¹	6-12 10 m ⁻² = 0.6 – 1.2 m ⁻² (Grigusova et al., 2021)	84.36 cm ²	0.67 m ³ ha ⁻¹ year ⁻¹
Continental	rodents	91.75g cm ⁻² = 3.75 cm ³ cm ⁻² (Imeson and Kwaad, 1976)	24.49 14 625 m ⁻² = 0.02 m ⁻² (Pang and Guo, 2017)	24.49 cm ² (Imeson and Kwaad, 1976)	0.183 m ³ ha ⁻¹ year ⁻¹
Temperate	mole crickets	22.1 g 115 cm ⁻² = 5.2 cm ³ cm ⁻² (Li et al., 2018)	405 ha ⁻¹ (Castner and Fowler, 1984)	115 cm ² (Li et al., 2018)	0.24 m ³ ha ⁻¹ year ⁻¹

Temperate	mole crickets	35.3 g cm ⁻² = 6.24 cm ³ cm ⁻² (Li et al., 2018)	220.5 405 ha ⁻¹ (Castner and al., 2018)	220.5 cm ² (Li et al., Fowler, 1984)	0.56 m ³ ha ⁻¹ year ⁻¹
Lab	chinese zocor	2,69 g cm ⁻² = 2.69 cm ³ cm ⁻² (Chen et al., 2021)	94.69 2500m ⁻² 400 ha ⁻¹	1256 cm ²	1.35 m ³ ha ⁻¹ year ⁻¹

697

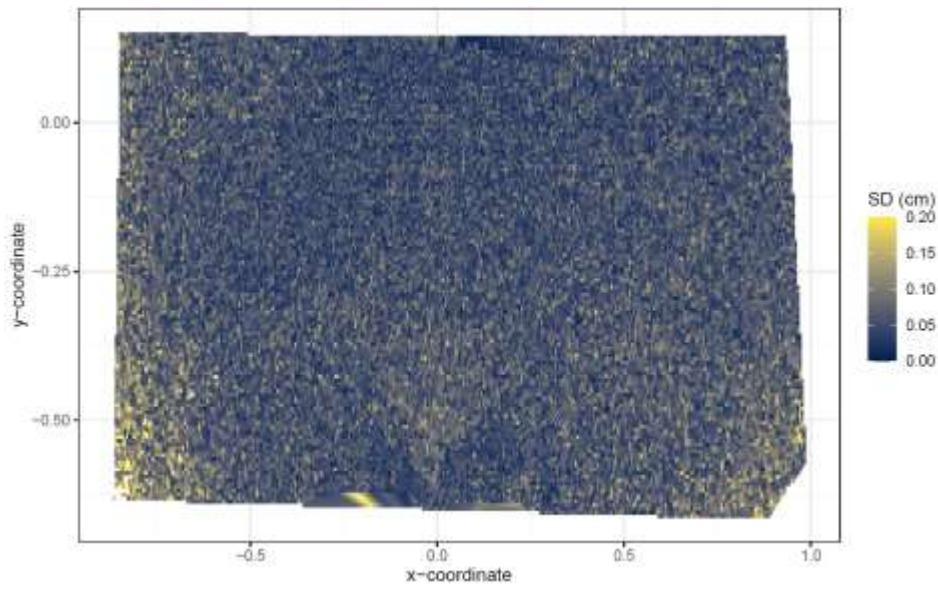
698

Table A8. Review of studies which estimated the volume of sediment excavated by burrowing animals.

	Climate	Animals	Method	Monitoring period	Frequency	volume of the excavated sediment
Our results	arid	vertebrates	Scanning	7 months	daily	0.18 m ³ ha ⁻¹ year ⁻¹
Our results	mediterranean	vertebrates	Scanning	7 months	daily	0.67 m ³ ha ⁻¹ year ⁻¹
(Black and Montgomery, 1991)	arid	porcupines	mound volume	3 years	yearly	0.2 m ³ ha ⁻¹ year ⁻¹
(Black and Montgomery, 1991)	arid	isopods	mound volume	3 years	yearly	0.11 m ³ ha ⁻¹ year ⁻¹
(Black and Montgomery, 1991)	arid	pocket gopher	mound volume	2 years	3 model runs	0.05 – 0.11 m ³ ha ⁻¹ year ⁻¹
(Rutin, 1996)	subtropical	scorpions	mound volume	6 months	2-29 days	0.42 m ³ ha ⁻¹ year ⁻¹
(Hall et al., 1999)	alpine	rodents	mound volume	1 year	yearly	0.02 m ³ ha ⁻¹ year ⁻¹
(Hall et al., 1999)	alpine	bears	mound volume	1 year	yearly	0.49 m ³ ha ⁻¹ year ⁻¹
(Yoo et al., 2005)	arid	pocket gopher	mound volume	1 year	One model run	0.1-0.2 m ³ ha ⁻¹ year ⁻¹

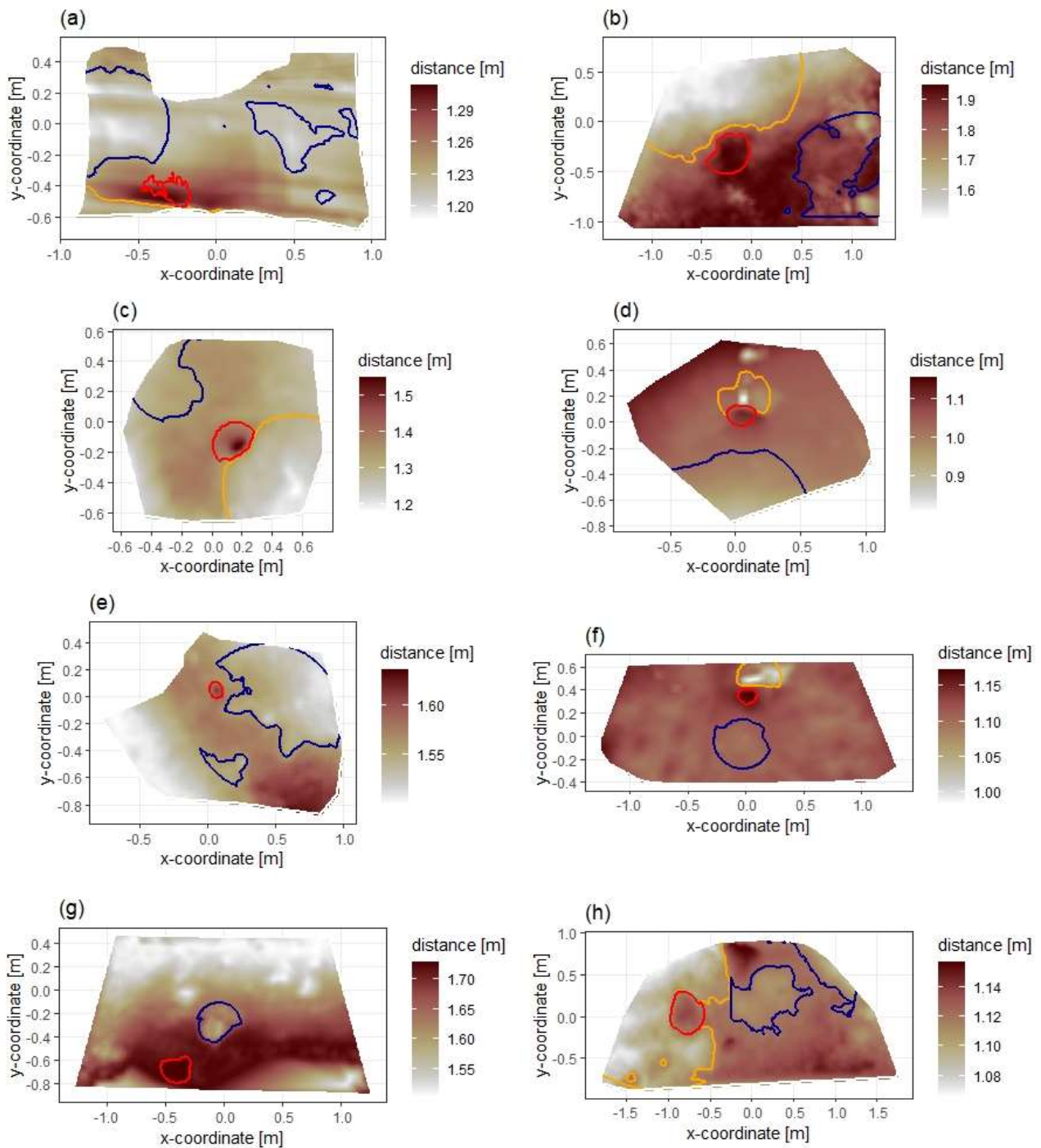
699

700



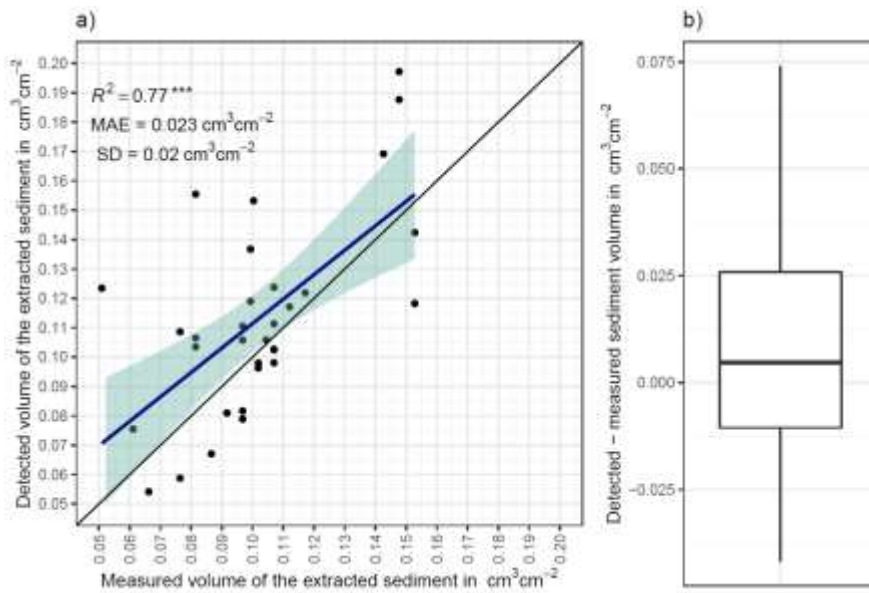
701
702
703
704
705
706

Figure A1. Standard deviation of the z-coordinate of unprocessed five scans showed exemplary for the camera on the upper north-facing hillside. SD is standard deviation. The error increases with distance from the camera nadir point. The standard deviation was here calculated from scans before any corrections.

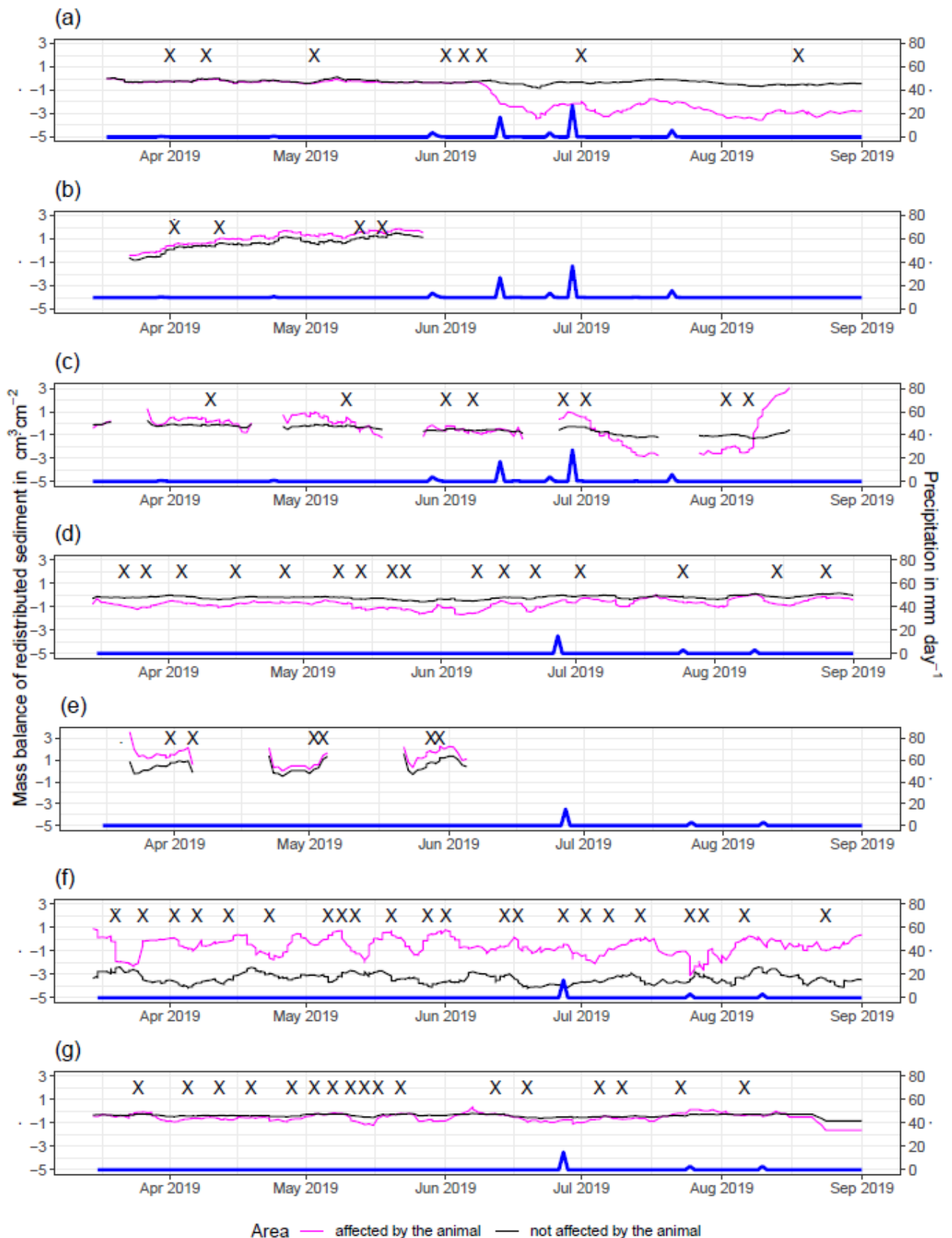


707

708 **Figure A2.** Delineation of the areas. The point of origin of the coordinate system is at the camera nadir. Depth
 709 is the distance between the surface and the camera. Red is the outline of the burrow entrance. Green is the
 710 outline of mound. Orange is the outline of burrow roof. Area which is not outlined is area not directly affected
 711 by the animal burrowing activity. Arrow indicates downhill direction of the hillslope. (a) LC-NU. (b) LC-NL (c)
 712 LC-SU. (d) LC-SL. (e) PdA-NU. (f) PdA-NL. (g) PdA-SU. (h) PdA-SL.



713
 714 **Figure A3.** a) Estimation of Time-of-Flight camera accuracy based on averaging two surface scans before and
 715 after the sediment extraction under controlled conditions. The x-axis shows the exact sediment volume
 716 measured with a cup. The y-axis represents the volume of the sediment calculated from the camera scans
 717 (according to Equation (4)). The blue line is the linear regression calculated from the measured and detected
 718 volume. The green shadow shows the confidence interval of 95% for the linear regression slope. $***p \leq 0.001$.
 719 MAE is the mean absolute error, SD is standard deviation and R^2 the coefficient of determination. b) Measured
 720 sediment volume subtracted from the detected sediment volume for all measurements.
 721



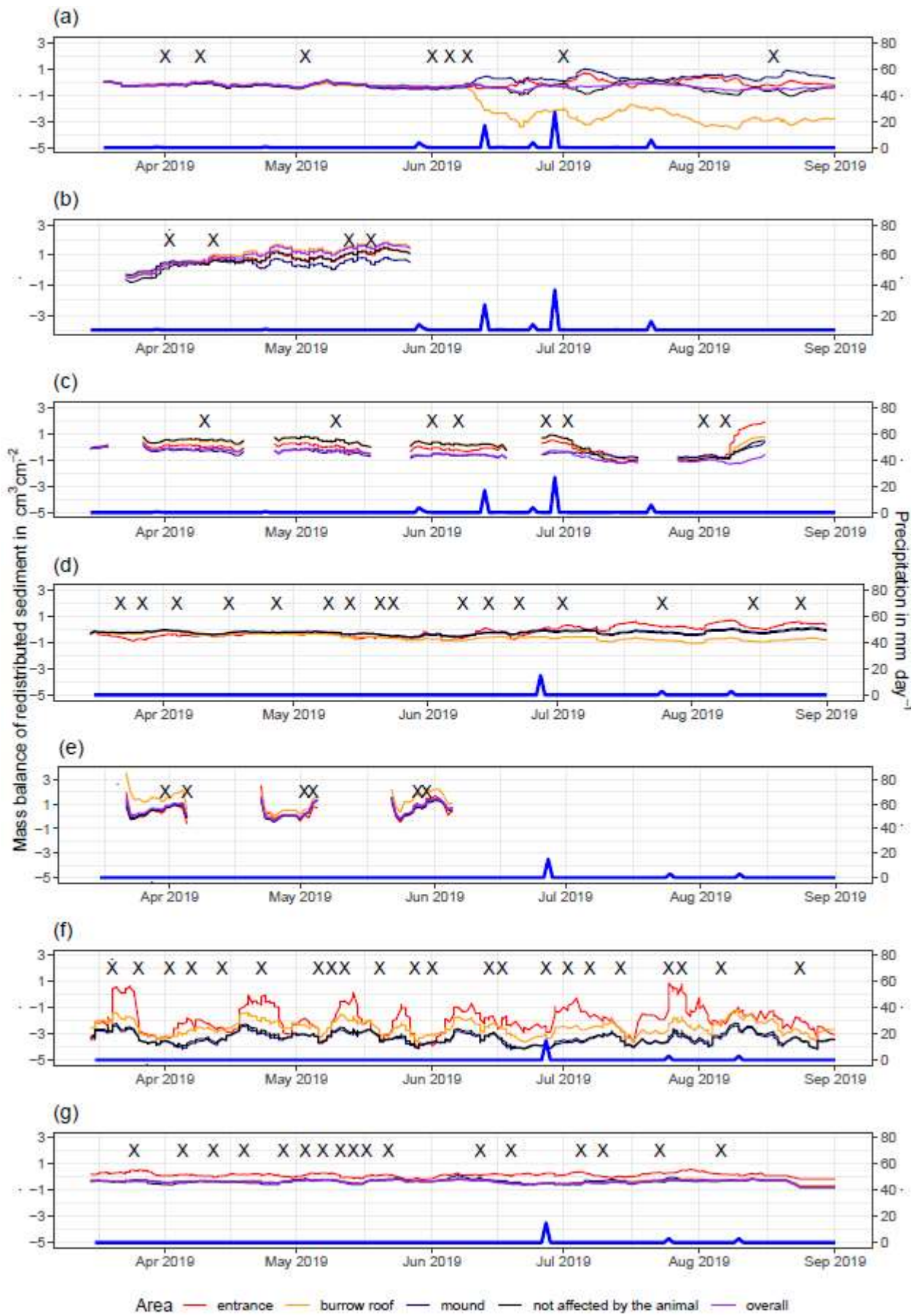
722

723

724

725

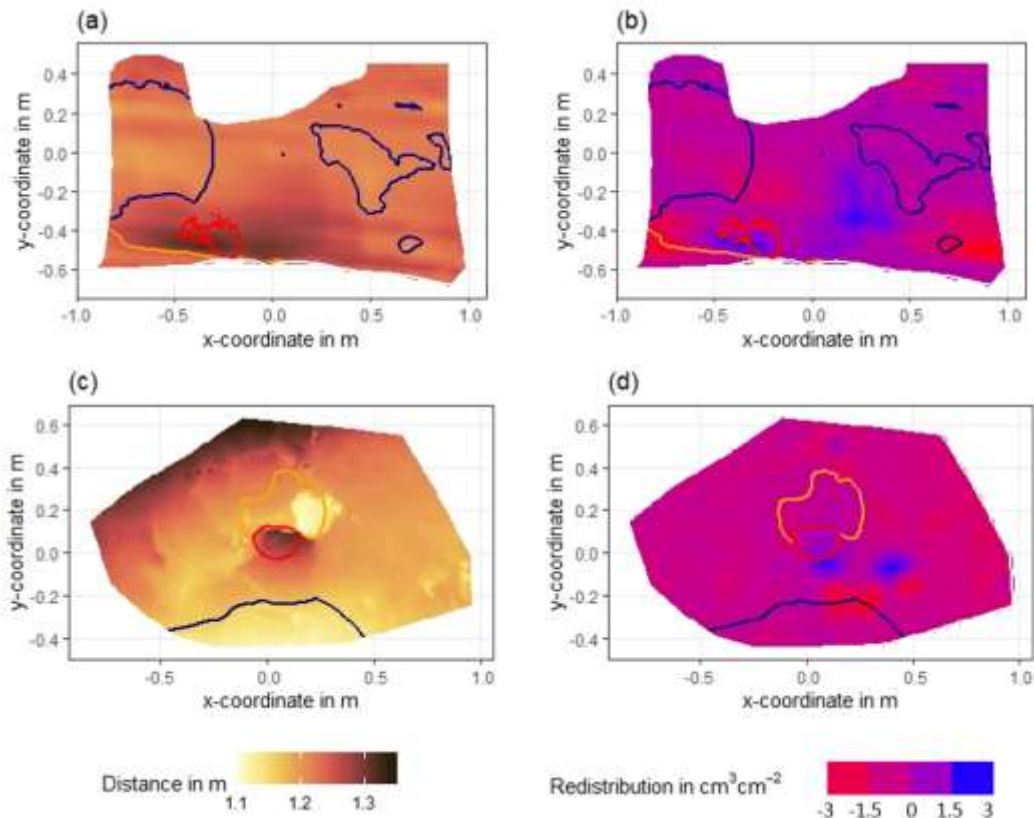
Figure A4. Sediment mass balance for the period of 7 months separately for areas affected and not affected by burrowing animal as measured by the cameras. (a) LC-NU. (b) LC-SU. (c) LC-SL. (d) PdA-NU. (e) PdA-NL. (f) PdA-SU. (g) PdA-SL. For abbreviations see Table A1.



726

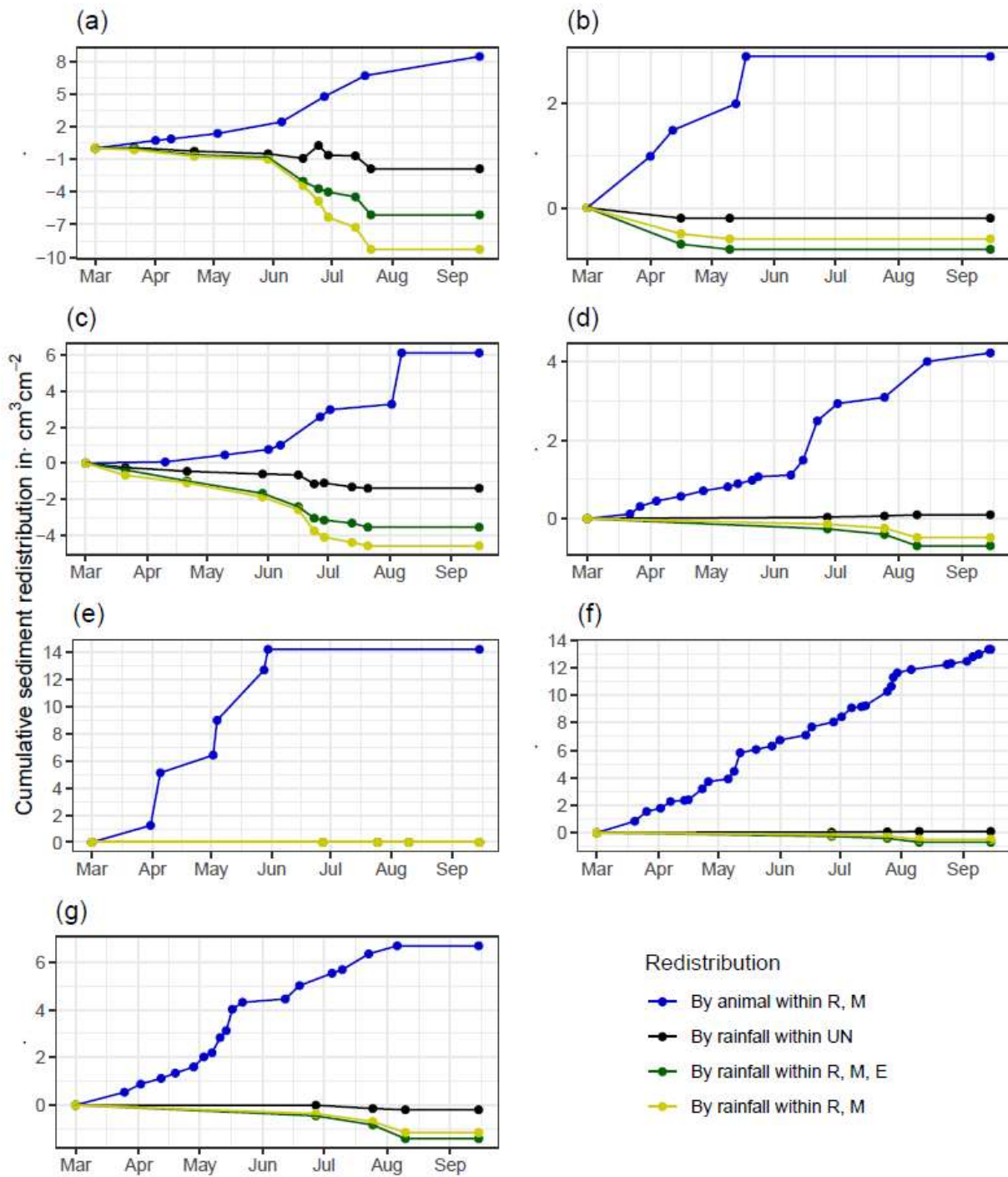
727 **Figure A5.** Sediment mass balance for the period of 7 months separately for all delineated areas as measured

728 by the cameras. (a) LC-NU. (b) LC-SU. (c) LC-SL. (d) PdA-NU. (e) PdA-NL. (f) PdA-SU. (g) PdA-SL. For
 729 abbreviations see Table A1.
 730

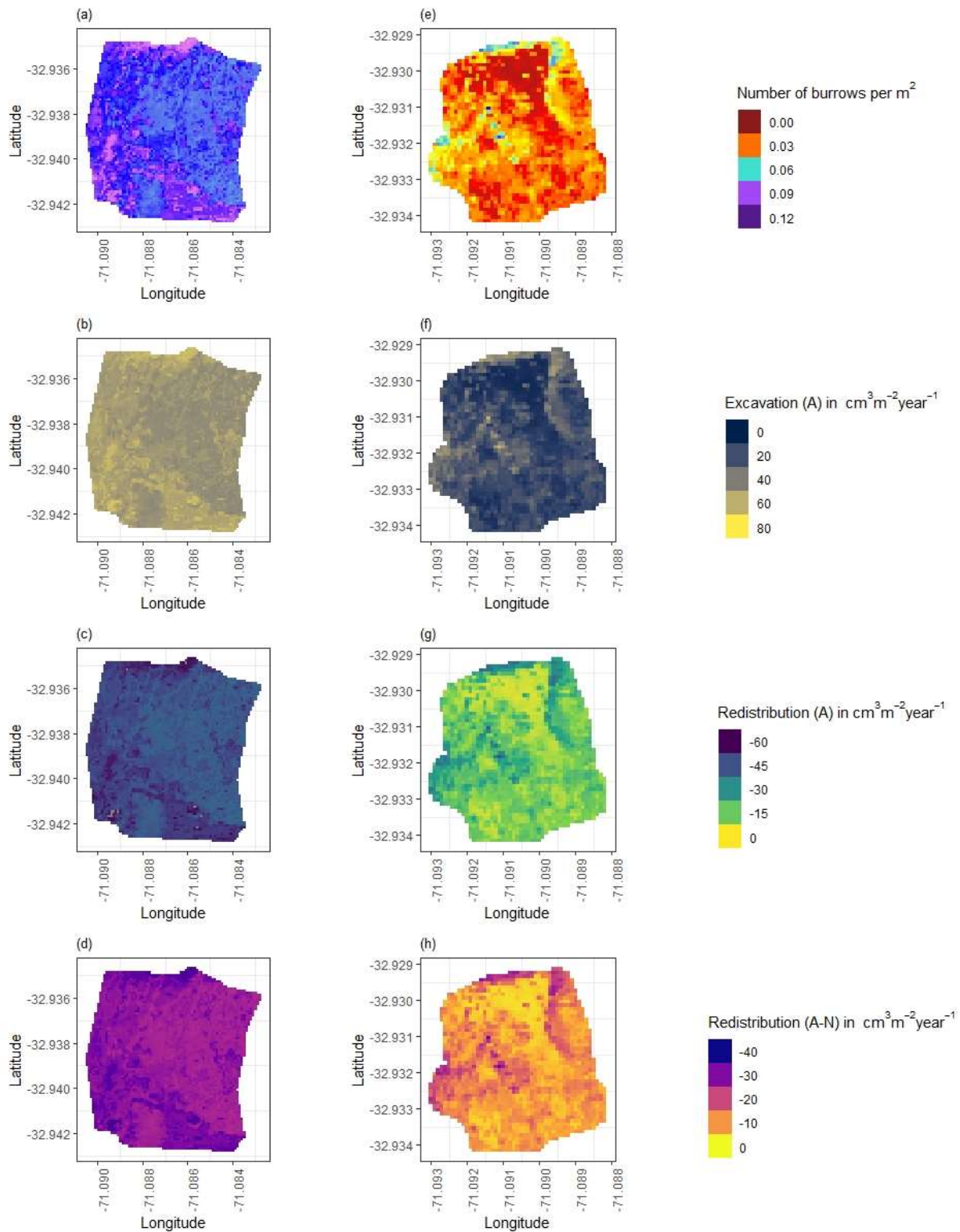


731
 732 **Figure A6.** Examples of surface scans showing the digital surface model (DSM) before a rainfall event (a, c)
 733 at two camera locations in La Campana, and the calculated volume of redistributed sediment (b, d) after the
 734 rainfall event: (a) DSM of a scan from the camera on the upper north-facing hillslope in La Campana; (b)
 735 Detected sediment redistribution ($\text{cm}^3 \text{cm}^{-2}$) on the upper north-facing hillslope in La Campana after a rainfall
 736 event of 17.2 mm day^{-1} ; (c) DSM of a scan from the camera on the upper south-facing hillslope in La Campana;
 737 (d) Detected sediment redistribution ($\text{cm}^3 \text{cm}^{-2}$) on the upper south-facing hillslope after a rainfall event of 17.2
 738 mm day^{-1} . Red is the outline of the burrow entrance. Green is the outline of mound. Orange is the outline of
 739 the burrow roof. The area which is not outlined is the area not directly affected by animal burrowing activity.
 740 Redistribution is the volume of the redistributed sediment, either accumulated (positive value) or eroded
 741 (negative value) per $\text{cm}^3 \text{cm}^{-2}$. After the rainfall events, sediment mostly accumulated within the burrow
 742 entrance or near mounds and eroded from burrow roofs and mounds.

743
 744

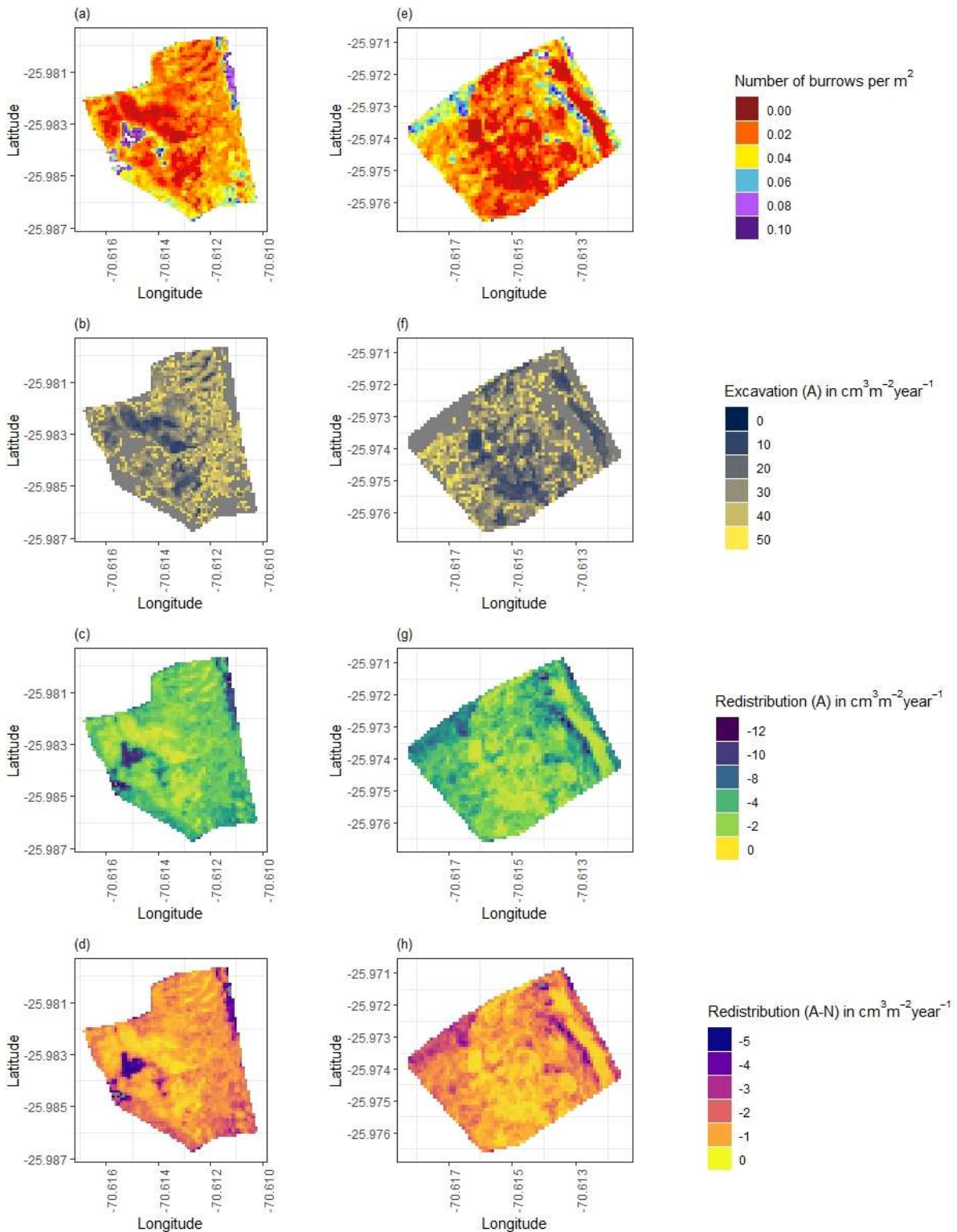


745
 746 **Figure A7.** Cumulative volume of redistributed sediment for all cameras. Positive values indicate sediment
 747 accumulation. Negative values indicate sediment erosion. Whiskers are the median sediment redistribution. E
 748 is the burrow entrance. M is the mound. R is burrow roof. UN is area not directly affected by the animal
 749 burrowing activity. LC is mediterranean climate zone. PdA is arid climate zone. (a) LC-NU. (b) LC-SU. (c) LC-
 750 SL. (d) PdA-NU. (e) PdA-NL. (f) PdA-SU. (g) PdA-SL. For abbreviations see Table A1.



751

752 **Figure A8.** Hillslope-wide volume of redistributed sediment for a time period of one year in LC. (a-d) North-
 753 facing hillslope. (e-h) South-facing hillslope. (a) and (e) Density of burrows as estimated by Grigusova et al.
 754 2021. (b) and (f) Volume of the sediment excavated by the animals. (c) and (g) Volume of the sediment
 755 redistributed during rainfall events within affected areas. (d) and (h) Volume of additionally redistributed
 756 sediment during rainfall events due to presence of the burrows. The values were calculated per burrow as
 757 stated in section 3.7 by subtracting the sediment volume redistributed within animal affected area from the
 758 sediment volume redistributed within not affected area and then upscaled. A stays for affected area, N stays
 759 for not affected area by the burrowing animal.



761

762 **Figure A9.** Hillslope-wide volume of redistributed sediment for a time period of one year in Pan de Azúcar. (a-
 763 d) North-facing hillslope. (e-h) South-facing hillslope. (a) and (e) Density of burrows as estimated by Grigusova
 764 et al. 2021. (b) and (f) Volume of the sediment excavated by the animals. (c) and (g) Volume of the sediment
 765 redistributed during rainfall events within affected areas. (d) and (h) Volume of additionally redistributed
 766 sediment during rainfall events due to presence of the burrows. The values were calculated per burrow as
 767 stated in section 3.7 by subtracting the sediment volume redistributed within animal affected area from the

768 sediment volume redistributed within not affected area and then upscaled. A stays for affected area, N stays
769 for not affected area by the burrowing animal.

770

771 References

- 772 Afana, A., Solé-Benet, A., and Pérez, J. L.: Determination of Soil Erosion Using Laser Scanners, last access:
773 22 December 2021, 2010.
- 774 Andersen, D. C.: *Geomys Bursarius* Burrowing Patterns: Influence of Season and Food Patch Structure,
775 *Ecology*, 68, 1306–1318, <https://doi.org/10.2307/1939215>, 1987.
- 776 Ashcroft, M. B., Gollan, J. R., and Ramp, D.: Creating vegetation density profiles for a diverse range of
777 ecological habitats using terrestrial laser scanning, *Methods Ecol Evol*, 5, 263–272,
778 <https://doi.org/10.1111/2041-210X.12157>, 2014.
- 779 BANCROFT, W. J., HILL, D., and ROBERTS, J. D.: A new method for calculating volume of excavated
780 burrows: the geomorphic impact of Wedge-Tailed Shearwater burrows on Rottneest Island, *Funct Ecology*,
781 18, 752–759, <https://doi.org/10.1111/j.0269-8463.2004.00898.x>, 2004.
- 782 Bernhard, N., Moskwa, L.-M., Schmidt, K., Oeser, R. A., Aburto, F., Bader, M. Y., Baumann, K.,
783 Blanckenburg, F. von, Boy, J., van den Brink, L., Brucker, E., Büdel, B., Canessa, R., Dippold, M. A.,
784 Ehlers, T. A., Fuentes, J. P., Godoy, R., Jung, P., Karsten, U., Köster, M., Kuzyakov, Y., Leinweber, P.,
785 Neidhardt, H., Matus, F., Mueller, C. W., Oelmann, Y., Osés, R., Osses, P., Paulino, L., Samolov, E.,
786 Schaller, M., Schmid, M., Spielvogel, S., Spohn, M., Stock, S., Stroncik, N., Tielbörger, K., Übernickel, K.,
787 Scholten, T., Seguel, O., Wagner, D., and Kühn, P.: Pedogenic and microbial interrelations to regional
788 climate and local topography: New insights from a climate gradient (arid to humid) along the Coastal
789 Cordillera of Chile, *CATENA*, 170, 335–355, <https://doi.org/10.1016/j.catena.2018.06.018>, 2018.
- 790 Black, T. A. and Montgomery, D. R.: Sediment transport by burrowing mammals, Marin County, California,
791 *Earth Surf. Process. Landforms*, 16, 163–172, <https://doi.org/10.1002/esp.3290160207>, 1991.
- 792 Blanch, X., Eltner, A., Guinau, M., and Abellan, A.: Multi-Epoch and Multi-Imagery (MEMI) Photogrammetric
793 Workflow for Enhanced Change Detection Using Time-Lapse Cameras, *Remote Sensing*, 13, 1460,
794 <https://doi.org/10.3390/rs13081460>, 2021.
- 795 Castner, J. L. and Fowler, H. G.: Distribution of Mole Crickets (Orthoptera: Gryllotalpidae: Scapteriscus) and
796 the Mole Cricket Parasitoid *Larra bicolor* (Hymenoptera: Sphecidae) in Puerto Rico, *The Florida*
797 *Entomologist*, 67, 481, <https://doi.org/10.2307/3494730>, 1984.
- 798 Cerqueira, R.: The Distribution of *Didelphis* in South America (Polyprotodontia, Didelphidae), *Journal of*
799 *Biogeography*, 12, 135, <https://doi.org/10.2307/2844837>, 1985.
- 800 Chen, M., Ma, L., Shao, M.'a., Wei, X., Jia, Y., Sun, S., Zhang, Q., Li, T., Yang, X., and Gan, M.: Chinese
801 zokor (*Myospalax fontanierii*) excavating activities lessen runoff but facilitate soil erosion – A simulation
802 experiment, *CATENA*, 202, 105248, <https://doi.org/10.1016/j.catena.2021.105248>, 2021.
- 803 Coombes, M. A.: Biogeomorphology: diverse, integrative and useful, *Earth Surf. Process. Landforms*, 41,
804 2296–2300, <https://doi.org/10.1002/esp.4055>, 2016.
- 805 Corenblit, D., Corbara, B., and Steiger, J.: Biogeomorphological eco-evolutionary feedback between life and
806 geomorphology: a theoretical framework using fossorial mammals, *Die Naturwissenschaften*, 108, 55,
807 <https://doi.org/10.1007/s00114-021-01760-y>, 2021.
- 808 Eitel, J. U.H., Williams, C. J., Vierling, L. A., Al-Hamdan, O. Z., and Pierson, F. B.: Suitability of terrestrial
809 laser scanning for studying surface roughness effects on concentrated flow erosion processes in
810 rangelands, *CATENA*, 87, 398–407, <https://doi.org/10.1016/j.catena.2011.07.009>, 2011.
- 811 Eltner, A., Schneider, D., and Maas, H.-G.: INTEGRATED PROCESSING OF HIGH RESOLUTION
812 TOPOGRAPHIC DATA FOR SOIL EROSION ASSESSMENT CONSIDERING DATA ACQUISITION
813 SCHEMES AND SURFACE PROPERTIES, *Int. Arch. Photogramm. Remote Sens. Spatial Inf. Sci.*, XLI-
814 B5, 813–819, <https://doi.org/10.5194/isprsarchives-XLI-B5-813-2016>, 2016a.
- 815 Eltner, A., Mulsow, C., and Maas, H.-G.: QUANTITATIVE MEASUREMENT OF SOIL EROSION FROM TLS
816 AND UAV DATA, *Int. Arch. Photogramm. Remote Sens. Spatial Inf. Sci.*, XL-1/W2, 119–124,
817 <https://doi.org/10.5194/isprsarchives-XL-1-W2-119-2013>, 2013.
- 818 Eltner, A., Kaiser, A., Abellan, A., and Schindewolf, M.: Time lapse structure-from-motion photogrammetry for
819 continuous geomorphic monitoring, *Earth Surf. Process. Landforms*, 42, 2240–2253,
820 <https://doi.org/10.1002/esp.4178>, 2017.
- 821 Eltner, A., Kaiser, A., Castillo, C., Rock, G., Neugirg, F., and Abellán, A.: Image-based surface reconstruction
822 in geomorphometry – merits, limits and developments, *Earth Surf. Dynam.*, 4, 359–389,
823 <https://doi.org/10.5194/esurf-4-359-2016>, 2016b.
- 824 Gabet, E. J., Reichman, O. J., and Seabloom, E. W.: The Effects of Bioturbation on Soil Processes and
825 Sediment Transport, *Annu. Rev. Earth Planet. Sci.*, 31, 249–273,
826 <https://doi.org/10.1146/annurev.earth.31.100901.141314>, 2003.
- 827 Galland, O., Bertelsen, H. S., Guldstrand, F., Girod, L., Johannessen, R. F., Bjugger, F., Burchardt, S., and

828 Mair, K.: Application of open-source photogrammetric software MicMac for monitoring surface
829 deformation in laboratory models, *J. Geophys. Res. Solid Earth*, 121, 2852–2872,
830 <https://doi.org/10.1002/2015JB012564>, 2016.

831 Grigusova, P., Larsen, A., Achilles, S., Klug, A., Fischer, R., Kraus, D., Übernicketel, K., Paulino, L., Pliscoff, P.,
832 Brandl, R., Farwig, N., and Bendix, J.: Area-Wide Prediction of Vertebrate and Invertebrate Hole Density
833 and Depth across a Climate Gradient in Chile Based on UAV and Machine Learning, *Drones*, 5, 86,
834 <https://doi.org/10.3390/drones5030086>, 2021.

835 Hakonson, T. E.: The Effects of Pocket Gopher Burrowing on Water Balance and Erosion from Landfill
836 Covers, *J. environ. qual.*, 28, 659–665, <https://doi.org/10.2134/jeq1999.00472425002800020033x>, 1999.

837 Hall, K., Boelhouwers, J., and Driscoll, K.: Animals as Erosion Agents in the Alpine Zone: Some Data and
838 Observations from Canada, Lesotho, and Tibet, *Arctic, Antarctic, and Alpine Research*, 31, 436–446,
839 <https://doi.org/10.1080/15230430.1999.12003328>, 1999.

840 Hancock, G. and Lowry, J.: Quantifying the influence of rainfall, vegetation and animals on soil erosion and
841 hillslope connectivity in the monsoonal tropics of northern Australia, *Earth Surf. Process. Landforms*, 46,
842 2110–2123, <https://doi.org/10.1002/esp.5147>, 2021.

843 Hänsel, P., Schindewolf, M., Eltner, A., Kaiser, A., and Schmidt, J.: Feasibility of High-Resolution Soil Erosion
844 Measurements by Means of Rainfall Simulations and SfM Photogrammetry, *Hydrology*, 3, 38,
845 <https://doi.org/10.3390/hydrology3040038>, 2016.

846 Hazelhoff, L., van Hoof, P., Imeson, A. C., and Kwaad, F. J. P. M.: The exposure of forest soil to erosion by
847 earthworms, *Earth Surf. Process. Landforms*, 6, 235–250, <https://doi.org/10.1002/esp.3290060305>,
848 1981.

849 Herbst, M. and Bennett, N. C.: Burrow architecture and burrowing dynamics of the endangered Namaqua
850 dune mole rat (*Bathyergus janetta*) (Rodentia: Bathyergidae), *Journal of Zoology*, 270, 420–428,
851 <https://doi.org/10.1111/j.1469-7998.2006.00151.x>, 2006.

852 Horn, B.K.P.: Hill shading and the reflectance map, *Proc. IEEE*, 69, 14–47,
853 <https://doi.org/10.1109/PROC.1981.11918>, 1981.

854 Imeson, A. C.: Splash erosion, animal activity and sediment supply in a small forested Luxembourg
855 catchment, *Earth Surf. Process. Landforms*, 2, 153–160, <https://doi.org/10.1002/esp.3290020207>, 1977.

856 Imeson, A. C. and Kwaad, F. J. P. M.: Some Effects of Burrowing Animals on Slope Processes in the
857 Luxembourg Ardennes, *Geografiska Annaler: Series A, Physical Geography*, 58, 317–328,
858 <https://doi.org/10.1080/04353676.1976.11879941>, 1976.

859 Iserloh, T., Ries, J. B., Arnáez, J., Boix-Fayos, C., Butzen, V., Cerdà, A., Echeverría, M. T., Fernández-
860 Gálvez, J., Fister, W., Geißler, C., Gómez, J. A., Gómez-Macpherson, H., Kuhn, N. J., Lázaro, R., León,
861 F. J., Martínez-Mena, M., Martínez-Murillo, J. F., Marzen, M., Mingorance, M. D., Ortigosa, L., Peters, P.,
862 Regúés, D., Ruiz-Sinoga, J. D., Scholten, T., Seeger, M., Solé-Benet, A., Wengel, R., and Wirtz, S.:
863 European small portable rainfall simulators: A comparison of rainfall characteristics, *CATENA*, 110, 100–
864 112, <https://doi.org/10.1016/j.catena.2013.05.013>, 2013.

865 James, M. R. and Robson, S.: Sequential digital elevation models of active lava flows from ground-based
866 stereo time-lapse imagery, *ISPRS Journal of Photogrammetry and Remote Sensing*, 97, 160–170,
867 <https://doi.org/10.1016/j.isprsjprs.2014.08.011>, 2014.

868 Jimenez, J. E., Feinsinger, P., and Jaksi, F. M.: Spatiotemporal Patterns of an Irruption and Decline of Small
869 Mammals in Northcentral Chile, *Journal of Mammalogy*, 73, 356–364, <https://doi.org/10.2307/1382070>,
870 1992.

871 Jones, C. G., Gutiérrez, J. L., Byers, J. E., Crooks, J. A., Lambrinos, J. G., and Talley, T. S.: A framework for
872 understanding physical ecosystem engineering by organisms, *Oikos*, 119, 1862–1869,
873 <https://doi.org/10.1111/j.1600-0706.2010.18782.x>, 2010.

874 Kaiser, A., Neugirg, F., Rock, G., Müller, C., Haas, F., Ries, J., and Schmidt, J.: Small-Scale Surface
875 Reconstruction and Volume Calculation of Soil Erosion in Complex Moroccan Gully Morphology Using
876 Structure from Motion, *Remote Sensing*, 6, 7050–7080, <https://doi.org/10.3390/rs6087050>, 2014.

877 Kinlaw, A. and Grasmueck, M.: Evidence for and geomorphologic consequences of a reptilian ecosystem
878 engineer: The burrowing cascade initiated by the Gopher Tortoise, *Geomorphology*, 157–158, 108–121,
879 <https://doi.org/10.1016/j.geomorph.2011.06.030>, 2012.

880 Kromer, R., Walton, G., Gray, B., Lato, M., and Group, R.: Development and Optimization of an Automated
881 Fixed-Location Time Lapse Photogrammetric Rock Slope Monitoring System, *Remote Sensing*, 11, 1890,
882 <https://doi.org/10.3390/rs11161890>, 2019.

883 Kukko, A. and Hyypä, J.: Small-footprint Laser Scanning Simulator for System Validation, Error
884 Assessment, and Algorithm Development, *photogramm eng remote sensing*, 75, 1177–1189,
885 <https://doi.org/10.14358/PERS.75.10.1177>, 2009.

886 Larsen, A., Nardin, W., Lageweg, W. I., and Bätz, N.: Biogeomorphology, quo vadis? On processes, time,
887 and space in biogeomorphology, *Earth Surf. Process. Landforms*, 46, 12–23,
888 <https://doi.org/10.1002/esp.5016>, 2021.

889 Le Hir, P., Monbet, Y., and Orvain, F.: Sediment erodability in sediment transport modelling: Can we account

890 for biota effects?, *Continental Shelf Research*, 27, 1116–1142, <https://doi.org/10.1016/j.csr.2005.11.016>,
891 2007.

892 Lehnert, L. W., Thies, B., Trachte, K., Achilles, S., Osses, P., Baumann, K., Schmidt, J., Samolov, E., Jung,
893 P., Leinweber, P., Karsten, U., and Büdel, B. Bendix, J.: A Case Study on Fog/Low Stratus Occurrence at
894 Las Lomitas, Atacama Desert (Chile) as a Water Source for Biological Soil Crusts, *Aerosol Air Qual.*
895 *Res.*, 18, 254–269, <https://doi.org/10.4209/aaqr.2017.01.0021>, 2018.

896 Li, G., Li, X., Li, J., Chen, W., Zhu, H., Zhao, J., and Hu, X.: Influences of Plateau Zokor Burrowing on Soil
897 Erosion and Nutrient Loss in Alpine Meadows in the Yellow River Source Zone of West China, *Water*, 11,
898 2258, <https://doi.org/10.3390/w11112258>, 2019a.

899 Li, L.: Time-of-Flight Camera – An Introduction, Technical White Paper,
900 <https://www.ti.com/lit/wp/sloa190b/sloa190b.pdf>, last access: 22 December 2021, 2014.

901 Li, T. C., Shao, M. A., Jia, Y. H., Jia, X. X., Huang, L. M., and Gan, M.: Small-scale observation on the effects
902 of burrowing activities of ants on soil hydraulic processes, *Eur J Soil Sci*, 70, 236–244,
903 <https://doi.org/10.1111/ejss.12748>, 2019b.

904 Li, T., Jia, Y., Shao, M.'a., and Shen, N.: *Camponotus japonicus* burrowing activities exacerbate soil erosion
905 on bare slopes, *Geoderma*, 348, 158–167, <https://doi.org/10.1016/j.geoderma.2019.04.035>, 2019c.

906 Li, T., Shao, M.'a., Jia, Y., Jia, X., and Huang, L.: Small-scale observation on the effects of the burrowing
907 activities of mole crickets on soil erosion and hydrologic processes, *Agriculture, Ecosystems &*
908 *Environment*, 261, 136–143, <https://doi.org/10.1016/j.agee.2018.04.010>, 2018.

909 Longoni, L., Papini, M., Brambilla, D., Barazzetti, L., Roncoroni, F., Scaioni, M., and Ivanov, V.: Monitoring
910 Riverbank Erosion in Mountain Catchments Using Terrestrial Laser Scanning, *Remote Sensing*, 8, 241,
911 <https://doi.org/10.3390/rs8030241>, 2016.

912 MALLALIEU, J., CARRIVICK, J. L., QUINCEY, D. J., SMITH, M. W., and JAMES, W. H.M.: An integrated
913 Structure-from-Motion and time-lapse technique for quantifying ice-margin dynamics, *J. Glaciol.*, 63,
914 937–949, <https://doi.org/10.1017/jog.2017.48>, 2017.

915 Meysman, F. J. R., Boudreau, B. P., and Middelburg, J. J.: Relations between local, nonlocal, discrete and
916 continuous models of bioturbation, *Journal of Marine Research*, 61, 391–410,
917 <https://doi.org/10.1357/002224003322201241>, 2003.

918 Morris, R. H., Buckman, S., Connelly, P., Dragovich, D., Ostendorf, B., and and Bradstock, R. A.: The dirt on
919 assessing post-fire erosion in the Mount Lofty Ranges: comparing methods, 2011.

920 Muñoz-Pedrerros, A., Yáñez, J., Norambuena, H. V., and Zúñiga, A.: Diet, dietary selectivity and density of
921 South American grey fox, *Lycalopex griseus*, in Central Chile, *Integrative zoology*, 13, 46–57,
922 <https://doi.org/10.1111/1749-4877.12260>, 2018.

923 Nasermoaddeli, M. B. and Pasche, E.: Application of terrestrial 3D scanner in quantification of the riverbank
924 erosion and deposition, [https://www.tuhh.de/t3resources/wb/Publikationen/MA-](https://www.tuhh.de/t3resources/wb/Publikationen/MA-Veroeffentlichungen/nasermoaddelli/riverflow2008.pdf)
925 [Veroeffentlichungen/nasermoaddelli/riverflow2008.pdf](https://www.tuhh.de/t3resources/wb/Publikationen/MA-Veroeffentlichungen/nasermoaddelli/riverflow2008.pdf), last access: 22 December 2021, 2008.

926 Pang, X. P. and Guo, Z. G.: Plateau pika disturbances alter plant productivity and soil nutrients in alpine
927 meadows of the Qinghai-Tibetan Plateau, China, *Rangel. J.*, 39, 133, <https://doi.org/10.1071/RJ16093>,
928 2017.

929 Reichman, O. J. and Seabloom, E. W.: The role of pocket gophers as subterranean ecosystem engineers,
930 *Trends in Ecology & Evolution*, 17, 44–49, [https://doi.org/10.1016/S0169-5347\(01\)02329-1](https://doi.org/10.1016/S0169-5347(01)02329-1), 2002.

931 Richards, P. J. and Humphreys, G. S.: Burial and turbulent transport by bioturbation: a 27-year experiment in
932 southeast Australia, *Earth Surf. Process. Landforms*, 21, n/a-n/a, <https://doi.org/10.1002/esp.2007>, 2010.

933 Ridd, P. V.: Flow Through Animal Burrows in Mangrove Creeks, *Estuarine, Coastal and Shelf Science*, 43,
934 617–625, <https://doi.org/10.1006/ecss.1996.0091>, 1996.

935 Romañach, S. S., Reichman, O. J., and Seabloom, E. W.: Seasonal influences on burrowing activity of a
936 subterranean rodent, *Thomomys bottae*, *Journal of Zoology*, 266, 319–325,
937 <https://doi.org/10.1017/S0952836905006941>, 2005.

938 Rutin, J.: The burrowing activity of scorpions (*Scorpio maurus palmatus*) and their potential contribution to
939 the erosion of Hamra soils in Karkur, central Israel, *Geomorphology*, 15, 159–168,
940 [https://doi.org/10.1016/0169-555X\(95\)00120-T](https://doi.org/10.1016/0169-555X(95)00120-T), 1996.

941 Sarbolandi, H., Plack, M., and Kolb, A.: Pulse Based Time-of-Flight Range Sensing, *Sensors (Basel,*
942 *Switzerland)*, 18, <https://doi.org/10.3390/s18061679>, 2018.

943 Schiffers, K., Teal, L. R., Travis, J. M. J., and Solan, M.: An open source simulation model for soil and
944 sediment bioturbation, *PLoS one*, 6, e28028, <https://doi.org/10.1371/journal.pone.0028028>, 2011.

945 Sharon, D.: The distribution of hydrologically effective rainfall incident on sloping ground, *Journal of*
946 *Hydrology*, 46, 165–188, [https://doi.org/10.1016/0022-1694\(80\)90041-4](https://doi.org/10.1016/0022-1694(80)90041-4), 1980.

947 Thomsen, L. M., Baartman, J. E. M., Barneveld, R. J., Starkloff, T., and Stolte, J.: Soil surface roughness:
948 comparing old and new measuring methods and application in a soil erosion model, *SOIL*, 1, 399–410,
949 <https://doi.org/10.5194/soil-1-399-2015>, 2015.

950 Übernickel, K., Pizarro-Araya, J., Bhagavathula, S., Paulino, L., and Ehlers, T. A.: Reviews and syntheses:
951 Composition and characteristics of burrowing animals along a climate and ecological gradient, Chile,

952 Biogeosciences, 18, 5573–5594, <https://doi.org/10.5194/bg-18-5573-2021>, 2021a.
953 Übernicketl, K., Ehlers, T. A., Paulino, L., and Fuentes Espoz, J.-P.: Time series of meteorological stations on
954 an elevational gradient in National Park La Campana, Chile, 2021b.
955 Voiculescu, M., Ianăș, A.-N., and Germain, D.: Exploring the impact of snow vole (*Chionomys nivalis*)
956 burrowing activity in the Făgăraș Mountains, Southern Carpathians (Romania): Geomorphic
957 characteristics and sediment budget, *CATENA*, 181, 104070,
958 <https://doi.org/10.1016/j.catena.2019.05.016>, 2019.
959 Wei, X., Li, S., Yang, P., and Cheng, H.: Soil erosion and vegetation succession in alpine Kobresia steppe
960 meadow caused by plateau pika—A case study of Nagqu County, Tibet, *Chin. Geograph.Sc.*, 17, 75–81,
961 <https://doi.org/10.1007/s11769-007-0075-0>, 2007.
962 Wilkinson, M. T., Richards, P. J., and Humphreys, G. S.: Breaking ground: Pedological, geological, and
963 ecological implications of soil bioturbation, *Earth-Science Reviews*, 97, 257–272,
964 <https://doi.org/10.1016/j.earscirev.2009.09.005>, 2009.
965 Yair, A.: Short and long term effects of bioturbation on soil erosion, water resources and soil development in
966 an arid environment, *Geomorphology*, 13, 87–99, [https://doi.org/10.1016/0169-555X\(95\)00025-Z](https://doi.org/10.1016/0169-555X(95)00025-Z), 1995.
967 Yoo, K., Amundson, R., Heimsath, A. M., and Dietrich, W. E.: Process-based model linking pocket gopher
968 (*Thomomys bottae*) activity to sediment transport and soil thickness, *Earth Surf. Process. Landforms*, 33,
969 917, <https://doi.org/10.1130/G21831.1>, 2005.
970